Author Manuscript

Author Manuscript

Author Manuscript

Author Manuscript

HHS Public Access

Author manuscript

*Cell Syst*. Author manuscript; available in PMC 2023 April 20.

Published in final edited form as:

*Cell Syst*. 2022 April 20; 13(4): 304–320.e5. doi:10.1016/j.cels.2022.01.005.

# Dynamics of huntingtin protein interactions in the striatum identifies candidate modifiers of Huntington's disease

**Todd M. Greco**[1], **Christopher Secker**[2], **Eduardo Silva Ramos**[2], **Joel D. Federspiel**[1], **Jeh-Ping Liu**[3], **Alma M. Perez**[5,6], **Ismael Al-Ramahi**[5,6], **Jeffrey P. Cantle**[4], **Jeffrey B. Carroll**[4], **Juan Botas**[5,6], **Scott O. Zeitlin**[3], **Erich E. Wanker**[2], **Ileana M. Cristea**[1,7,*]

[1]Department of Molecular Biology, Princeton University, Washington Road, Princeton, NJ USA

[2]Neuroproteomics, Max Delbrück Centre for Molecular Medicine, Berlin, Germany.

[3]Department of Neuroscience, University of Virginia School of Medicine, Charlottesville, VA USA

[4]Department of Psychology, Western Washington University, Bellingham, WA USA

[5]Jan and Dan Duncan Neurological Research Institute, Houston, Texas, USA

[6]Department of Molecular and Human Genetics, Baylor College of Medicine, Houston, Texas USA

[7]Lead contact

## Summary

Huntington's disease (HD) is a monogenic neurodegenerative disorder with one causative gene, huntingtin (HTT). Yet, HD pathobiology is multifactorial, suggesting that cellular factors influence disease progression. Here, we define HTT protein-protein interactions (PPIs) perturbed by the mutant protein with expanded polyglutamine in the mouse striatum, a brain region with selective HD vulnerability. Using metabolically labeled tissues and immunoaffinity purification-mass spectrometry, we establish that polyglutamine-dependent modulation of HTT PPI abundances and relative stability starts at an early stage of pathogenesis in a Q140 HD mouse model. We identify direct and indirect PPIs that are also genetic disease modifiers using in-cell two-hybrid and behavioral assays in HD human cell and *Drosophila* models, respectively. Validated, disease-relevant mHTT-dependent interactions encompass mediators of synaptic neurotransmission (SNAREs and glutamate receptors) and lysosomal acidification (V-ATPase). Our study provides a resource for understanding mHTT-dependent dysfunction in cortico-striatal cellular networks

*Correspondence: Ileana M. Cristea (icristea@princeton.edu), 210 Lewis Thomas Laboratory, Department of Molecular Biology, Princeton University, Princeton, NJ 08544, Tel: 6092589417, Fax: 6092584575.

Author contributions

TMG and IMC conceived and led the study, wrote the manuscript, and all authors contributed to the manuscript. J-PL and SOZ bred the HD mouse models and dissected brain tissues. TMG, JDF, and IMC conceived and designed the IP-MS experiments. TMG performed and analyzed the IP-MS experiments. CS, ESR, EW designed and ESR and CS performed the LuTHy experiments and the data analysis. JB, JPC, and JBC conceived, AMP performed, and IA-R performed, designed, and analyzed the *Drosophila* motor performance assays.

**Publisher's Disclaimer:** This is a PDF file of an unedited manuscript that has been accepted for publication. As a service to our customers we are providing this early version of the manuscript. The manuscript will undergo copyediting, typesetting, and review of the resulting proof before it is published in its final form. Please note that during the production process errors may be discovered which could affect the content, and all legal disclaimers that apply to the journal pertain.

Declaration of interests

We have no conflicts of interest to declare.

Author Manuscript Author Manuscript Author Manuscript Author Manuscript

partly through impaired synaptic communication and endosomal-lysosomal system. A record of this paper's Transparent Peer Review process is included in the Supplemental Information.

## Graphical Abstract

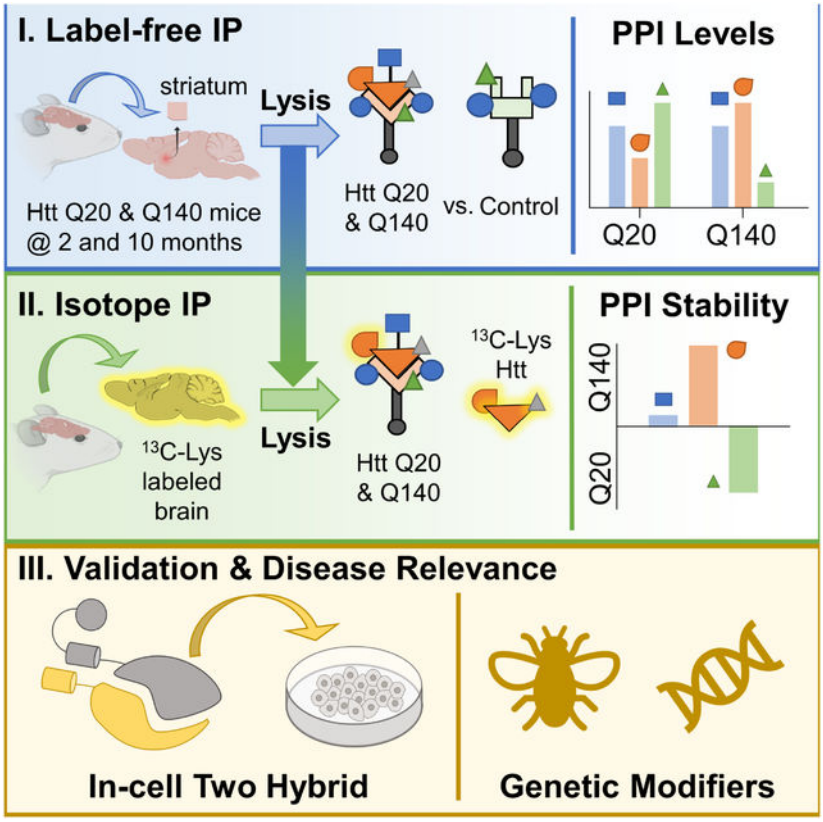


## eTOC Blurb

No therapy has been approved to slow Huntington's disease (HD) progression. Here, we profiled the perturbation of protein interaction levels and stabilities due to mutant huntingtin in HD mice. High value disease modifier candidates were pinpointed by their persistence in human cells and impact on motor performance in HD flies.

### Keywords

immunoaffinity purification mass spectrometry; protein interactions; label-free quantification; metabolic labeling; vesicle trafficking; SNARE; Arp2/3; AMPA receptors; LuTHy; D. melanogaster; synaptic biology

## Introduction

Huntington's disease (HD) is an autosomal dominant neurodegenerative disorder that clinically manifests with progressive motor dysfunction and cognitive abilities, and increases in psychiatric issues (Bates et al., 2015). In contrast to Alzheimer's and Parkinson's

Author Manuscript Author Manuscript Author Manuscript Author Manuscript

diseases, HD is a monogenic disorder, caused by a trinucleotide CAG repeat expansion in exon 1 of the huntingtin (*HTT*) gene (MacDonald et al., 1993). The number of CAG repeats is inversely correlated with the onset of clinical symptoms (Ross and Tabrizi, 2011). The CAG expansion results in a mutant protein (mHTT) with an expanded tract of glutamine (polyQ) residues located at the N-terminus of HTT. mHTT is widely expressed in most tissues, yet neurodegeneration is selective (Carroll et al., 2015; MacDonald and Gusella, 1996; Vonsattel, 2008). The predominant neuropathological phenotype in HD patients is a corticostriatal degeneration of white and gray matter, with selective loss of medium spiny neurons in the striatum and pyramidal neurons in the cortex (Waldvogel et al., 2014). Neuroimaging studies show that the loss of grey matter and white matter tracts occurs prior to disease onset (Ciarochi et al., 2019; Poudel et al., 2019). Consistent with this observation, the cellular pathobiology of HD precedes the onset of clinical symptoms (Ross and Tabrizi, 2011). These features of HD can be recapitulated in HD mouse models, where abnormal protein processing and aggregation, and impairment of cellular homeostasis have been documented prior to the development of symptoms (Ast et al., 2018; Hodgson et al., 1999; Schilling et al., 1999). Indeed, the pathogenic potential of mHTT is consequential given the wild-type protein has been implicated in diverse cellular processes, including autophagy, endocytosis, vesicular trafficking, synaptic transmission, mitochondria homeostasis, transcription/translation (reviewed in Saudou et al., 2016), and more recently, DNA repair (Gao et al., 2019; Maiuri et al., 2019). Cellular processing of full length mHTT leads to production of N-terminal mHTT fragments containing the expanded polyQ tract, which can readily self-aggregate (DiFiglia et al., 1997; Scherzinger et al., 1997), and form higher order structures, including oligomers (Kim et al., 2016), β-sheet rich amyloid fibrils (Scherzinger et al., 1999), and ultimately, large insoluble aggregates. The role of these distinct molecular assemblies as disease drivers or in maintaining cellular homeostasis is an active area of research (Wanker et al., 2019). The early molecular changes that are initiated by mHTT and how these changes are propagated across signaling networks to promote cellular dysfunction remain incompletely understood. Therefore, while HD etiology is monogenic, HD pathobiology is complex and likely involves disease-modifying factors that have unique roles in specific brain regions.

Cell type specific regulation of protein complex dynamics is one potential disease-modifying factor. A single protein can participate in different biological processes as a component of distinct protein complexes (Antonicka et al., 2020; Banks et al., 2020; Joshi et al., 2013). These functional protein assemblies can be spatially and temporally regulated within a cell and may contain numerous protein interactions with a range of dynamic properties from stable to transient (Budayeva and Cristea, 2014; Hashimoto et al., 2020; Liu et al., 2016; Przytycka et al., 2010). The majority of human diseases are associated with dysregulation of protein interactions (Bergendahl et al., 2019; Vanunu et al., 2010), which can be linked to alterations in protein localization, folding, posttranslational modifications, and abundance (Jean Beltran et al., 2017; Lapek et al., 2017; Nishi et al., 2013). Therefore, identifying disease-modulated protein interactions in the context of HD can provide insights into affected cellular pathways and targets for therapeutic interventions (Kaltenbach et al., 2007). Given that HTT is a relatively large protein (~350 kDa) with unique conformational states (see above), it is not surprising that previous studies have found numerous interacting

Author Manuscript Author Manuscript Author Manuscript Author Manuscript

partners, which have been curated in the HD explorer portal (Aaronson et al., 2021; Wanker et al., 2019). This knowledge was primarily accrued through large-scale two-hybrid and mass spectrometry-based approaches (Culver et al., 2012; Goehler et al., 2004; Kaltenbach et al., 2007; Kim et al., 2016; Ratovitski et al., 2012; Ripaud et al., 2014; Shirasaki et al., 2012; Tourette et al., 2014; Wang et al., 2009; Zhao et al., 2018). Together, experimental and bioinformatics strategies have driven the discovery of functionally relevant HTT PPIs. For example, HAP40 (F8A1) was found to co-purify with HTT in human cells and mouse tissues (Peters and Ross, 2001), and recent structural studies have established that this protein represents a direct HTT interacting partner, binding primarily to the latter's HEAT domains (Guo et al., 2018; Harding et al., 2019). The HTT/HAP40 complex was shown to participate in endocytosis as a Rab5 effector and was linked to dysfunctional endosomal dynamics in striatal cells isolated from an HD mouse model (Pal et al., 2006). PPI studies have also provided evidence of mHTT-dependent interactions with proteins that have roles in axonal transport, autophagy, and transcription (reviewed in (Wanker et al., 2019)). While these studies have provided new insights into HTT protein functions, it remains unknown which HTT interactions are proximal modulators of disease progression. A systematic, quantitative assessment of HTT PPI polyQ dependency in disease relevant brain regions, such as the striatum, is lacking.

Quantitative proteomic approaches are well suited for understanding the multi-factorial regulation of PPIs. To uncover the dynamics of protein interactions, our group has previously designed a complementary immunoaffinity purification approach using parallel label-free and isotope-labeled quantitative mass spectrometry, which we applied to investigate lysine deacetylases in T cells (Joshi et al., 2013). The integration of label-free and metabolic labeling IP-MS allowed us to determine PPI specificity and relative stability, i.e., stable versus transient/on-off associations. Here, we have further developed this approach to transition it from cell culture systems to animal models by using heavy isotope-labeled mouse brain tissue. Using this strategy in an HD mouse model containing an expanded Htt-Q140 polyglutamine stretch, we identified striatal-derived Htt PPIs that are altered in their interaction levels and/or stability at early and later stages of HD pathogenesis. In addition, we validate and further support the disease relevance of identified polyQ length-dependent striatal PPIs using bioluminescence-based two-hybrid assays in a human HD cell model and behavioral assays in an HD fly model. Overall, our study pinpoints Htt interactions that are polyQ-dependent, identifying direct and indirect binding partners, as well as genetic modifiers, and providing a resource for future studies on the regulation of cellular pathways during HD.

## Results

### The levels and functional classes of mHtt protein interactions in the striatum are unique to the disease state.

We investigated the protein interaction landscape of Htt from the degenerating striatum as a function of polyQ and disease state in a knock-in HD mouse model (Zheng et al., 2012) (Fig 1A–B). The HD mouse model contained knock-in of an N-terminal 3xFLAG epitope tag and human HTT exon1 with either a normal (Q20) or expanded (Q140) polyglutamine

Author Manuscript Author Manuscript Author Manuscript Author Manuscript

(polyQ) tract. An expanded polyQ of this length has been shown to cause behavioral and neuropathological phenotypes in mice similar to the human disease (Hickey et al., 2008; Menalled et al., 2003). HD mice were evaluated at 2- (2m) and 10-months of age (10m), which were selected to represent an early and later stage of Q140 HD mouse model pathogenesis. The FLAG-tagged variants have no apparent abnormalities compared to untagged mice and have been successfully used to isolate Htt-containing complexes from whole brain of juvenile mice (Culver et al., 2012). The FLAG tag allowed integration of label-free and metabolic labeling immunoaffinity purification-mass spectrometry (IP-MS) (Greco et al., 2016; Tackett et al., 2005).

We first employed label-free immunoaffinity purification to determine the specificity of Htt interacting partners and their polyQ-dependence (Fig 1A & B, *top*). To optimize isolation of FLAG-Htt, we performed pilot IP experiments in whole brain. Following tissue disruption and solubilization, the yield of FLAG-Htt in soluble fractions from $Htt^{3xFlagQ20/+}$ (Q20) and $Htt^{3xFlagQ140/+}$ (Q140) tissues in 2-month mice was >95%, and anti-FLAG immunoisolation showed adequate efficiency (~70%) as assessed by western blotting (Fig 1C and S1A). As an additional control, we confirmed that mHtt from Q140 tissues was co-isolated with its known high-affinity interacting partner, Hap40 (Peters and Ross, 2001), and both were enriched >1000-fold compared to control isolations (Fig 1D, *WB*).

Given these confirmatory results, we proceeded to isolate Htt complexes from the striatum, the region of the brain that is most affected in HD (Waldvogel et al., 2014). Htt was isolated from striatal tissues dissected from Q20 and Q140 mice at 2m and 10m. The ability to isolate soluble FLAG-Htt was not affected by polyQ length or disease stage (Fig S1B). Similar to whole brain, Hap40 was co-isolated with Htt from the striatum (Fig 1E). We observed a modest polyQ-dependent relative increase in the Hap40 association (~40%) at 2m, but not at 10m (Fig 1E). Other previously identified Htt interactions were detected, including the mitochondrial phosphate carrier protein (Slc25a3) and contactin-1 (Cntn1) (Kaltenbach et al., 2007; Shirasaki et al., 2012), the former of which was a genetic disease modifier in an HD transgenic fly model (Shirasaki et al., 2012). The interaction levels of these proteins showed an increasing polyQ length-dependent trend, with significance for Cntn1 at 10m (Fig 1E).

Having confirmed the enrichment of known Htt interactions in the FLAG IPs, we performed computational analysis of all co-isolated proteins to establish a broader pool of candidate Htt PPIs (Fig 1B, *top*). Prior to specificity filtering, the numbers and abundance distributions of proteins were similar across IP samples (630±9 proteins, Fig S1D–E). Interaction specificity was assessed by SAINT, a probabilistic scoring algorithm for affinity purification datasets (Choi and Nesvizhskii, 2008; Choi et al., 2011). Based on the overall score distributions and the scores of previously detected Htt interactions (Aaronson et al., 2021)(Fig S2A–D), a SAINT probability of > 0.80 was selected to assign putative HTT interaction candidates. A total of 278 proteins passed this score threshold in at least one sample group (Table S1 and Fig S1D), 72 of which have not been previously annotated as HTT interacting proteins (Aaronson et al., 2021). SAINT PPI scoring is based on spectral counting; however, as spectral counts are weak measures of protein abundance, differential Htt interactions were determined using intensity-based quantification of PPI abundances (Fig S1F, Table S2).

Author Manuscript Author Manuscript Author Manuscript Author Manuscript

Using principal component analysis, abundance profiles of quantified PPIs clustered closely within biological replicates, while sample groups demonstrated polyQ dependency (Fig 1G). We next visualized the degree and pattern of interaction changes as a function of expanded polyQ and age using hierarchical clustering analysis (Fig 2A). Four of the nine resulting clusters contained the majority of proteins, which represented increasing interaction levels (Fig 2A & 2B).

Within the polyQ-dependent clusters, clusters 1 and 2 had the largest relative increases at 2m. PPIs in these clusters are over-represented in synaptic transmission and signal transduction associated Reactome pathways (Fig 2C, *top*, and S2E). The functional interaction network assembled using STRING database relationships (Szklarczyk et al., 2017) contains an interconnected module of SNAREs and associated proteins (Nsf, Snap25, Syn1, Syn2), which regulate vesicle trafficking and fusion. Also detected were proteins that participate in WNT and $G_i$alpha signaling, including protein kinases (Prkcg, Prkar2b, Csnk2a1), phosphatases (PP2A subunits), and other signaling proteins (Gnb5, Pmch) (Fig 3A). The interaction abundances with mHtt were consistently >2-fold relative to the control (Q20), with the largest increase observed for the vesicle-fusing ATPase Nsf (>50-fold). Clusters 5, 6, and 7 had more modest polyQ-dependent increases at 2-months, but robust increases at 10-months (usually >6-fold) (Fig 2A–B). Proteins within these clusters function in synapse morphogenesis and regulation of the actin cytoskeleton (Fig 2C, *middle & bottom*, Fig S2E, & Fig 3B). A smaller subset of proteins shows opposite patterns (clusters 8 & 9) with interactions that are on average decreased due to expanded polyQ; however, the abundance patterns of PPIs in cluster 8 were less uniform.

To gain further confidence in individual PPI alterations, we next evaluated their polyQ and age dependence by statistical significance and magnitude of change (Fig 3C–D). PPIs with an average log2 fold-change $\geq \pm 1.0$ and associated p-value $\leq 0.05$ were considered polyQ length-dependent. As a control, several Htt PPIs found in previous mouse IP-MS studies to be largely independent of polyQ length at 2m (Culver et al., 2012; Shirasaki et al., 2012) were similarly not significantly modulated in our data, including AP2A1, CNTN1 (Fig 1E), HSP90AB1, HSP90AA1, HSPA12A, SYT1, VDAC1, and VDAC3. Using the above criteria, most of the polyQ-dependent PPIs in 2m mice were found to be increased in association with mHtt (113 of 123), with only 10 PPIs displaying decreased interaction (Fig 3C). In 10m mice, all significantly mHtt perturbed interacting partners (139 PPIs) were increased in interaction levels (Fig 3D). The number of unique and shared high confidence polyQ-dependent PPIs were similar between 2m and 10m mice (*Venn diagram* in Fig 3C–D, and Table S2).

We next evaluated whether polyQ-independent factors may contribute to modulation of Htt PPIs. Analysis of age-dependent (10m vs. 2m) PPIs in control (Q20) mice found only 34 differential PPIs (Fig S3A–B), suggesting the majority of polyQ-dependent PPIs (Fig 3C) were not age-dependent. However, within the age-dependent interactions, the majority were also polyQ-dependent (Fig S3B). It is also possible that differential PPIs are driven by changes in the proteome or transcriptome. A prior study profiled mRNA and protein levels across tissues from *Htt* knock-in HD mouse models with a range of CAG repeat lengths and at different ages (Langfelder et al., 2016). Using this resource from Langfelder

Author Manuscript Author Manuscript Author Manuscript Author Manuscript

et al. (see Methods, PXD003442), we previously re-analyzed the striatal proteomes of Q140 and Q20 mice at 2m and 10m (Federspiel et al., 2019) using the same label-free quantification method as for the IP-MS experiments. Based on these omics measurements, the vast majority of polyQ-dependent PPIs were not altered at the proteome or transcriptome level in either 2m or 10m mice (Fig S3). These results suggest that polyQ-dependent differential PPIs are largely associated with the underlying biochemical changes caused by gain or loss of function of polyQ expansion, and only a minority of polyQ-dependent PPIs may involve an accelerated aging phenotype or regulation through transcription and/or translation. Of note, a previous comparison of coexpression network modules between these transcriptome and proteome datasets and Htt PPIs in BACHD mice (Shirasaki et al., 2012) showed a functional overlap (Veldman and Yang, 2018). Taken together, this suggests that mHTT-dependent interactome remodeling and transcriptome/proteome dysregulation converge on shared cellular pathways but may have different temporality and/or have distinct molecular targets.

## The stability landscape of Htt protein interactions in the striatum reveals a dichotomy in stabilization between early and later stages of pathogenesis in HD mice

Our identification of polyQ-dependent proteins associated with mHtt (Table S2) suggested that interactome remodeling is a prominent feature of HD mouse model pathogenesis. Yet, based on differential interaction levels alone, it remains challenging to determine protein interactions that are most proximal to disease progression. Towards this goal, we adapted the complementary isotope-labeling IP-MS approach (Joshi et al., 2013) to use mouse brain tissues with $^{13}$C-lysine incorporation for investigating alterations in Htt interaction stabilities resulting from expanded polyQ (Fig 1A–B, *bottom*). Heavy ($^{13}$C)-labeled wild-type brains were age-matched to FLAG-Htt control and HD mice and the corresponding lysates were mixed 1:1 (w:w). FLAG-Htt was affinity purified from the mixed lysate and co-isolated proteins were quantified by their light and heavy isotopes using mass spectrometry (Fig 1A, *bottom*). An identified interaction was considered relatively stable when the isotope ratio, i.e., $^{12}$C (endogenous) / [$^{12}$C (endogenous) + $^{13}$C (reference)] approached one, indicating the candidate PPI did not exhibit in-solution exchange during the isolation. In contrast, isotope ratios nearer to 0.5 represented likely fast-exchanging or transient associations. By combining this isotope-labeled workflow with our label-free IP-MS, we gained a profile of Htt interaction dynamics (Fig 1B).

Given that this approach for assessing interaction dynamics has previously been demonstrated only in cellular models (Greco et al., 2016; Joshi et al., 2013; Tackett et al., 2005) and not in tissues, we first evaluated the reproducibility of isotope-labeled IP-MS experiments. A higher correlation between isotope protein ratios from biological duplicates was observed compared to those between different biological samples (Fig S4B, red boxes). A slight reduction in correlation for 10m versus 2m samples was seen, but this was not polyQ-dependent. This difference may be connected to the lower signal of endogenous PPIs at 10m. Overall, relative stability measurements were obtained for 72% (201 / 278) of the candidate Htt PPIs that were also quantified by label-free IP-MS experiments (Table S3).

Author Manuscript Author Manuscript Author Manuscript Author Manuscript

To define the stability landscape of Htt PPIs, we next compared the isotope ratios, herein referred to as stability ratios (SR), to the average specificity scores from the label-free IP-MS experiments (Fig 4A). Proteins passing the specificity criteria were assigned as interactors that are stable (upper-right quadrant) or decreased in stability (upper-left, SR<0.8) (Fig 4B – C). The structurally characterized Htt interaction, Hap40, was consistently stable (SR = 1), being independent of mHtt and disease stage. The change in the number of proteins in these quadrants between conditions suggests a shift in the stability landscape of Htt interactions. The number of specific and stable proteins increased from 72 to 106 as a function of polyQ length in 2m mice (Fig 4B, *left vs right*), suggesting an overall stabilizing effect of expanded polyQ. At 10m, we also observed a polyQ-dependent increase in the number specific and stable PPIs (24 to 36) (Fig 4D, *left vs right*), though the absolute number of proteins in these quadrants was lower compared to the 2m age. In addition, the comparison of the stability landscape in Q20 mice at 2m vs. 10m suggests an age-dependent effect (Fig 4B vs C, *Q20*). The polyQ-dependent increase in the number of stable PPIs was consistent with the upward shift in the distribution of protein SR (Fig S4C), which showed a statistically significant polyQ-dependent increase for 2m, but not 10m mice.

Next, we calculated the SR difference (ΔSR) between Q140 and Q20 to provide a quantitative metric for the effect of expanded polyQ on interaction stability. Positive and negative ΔSR values reflected increased or decreased relative stability, respectively. The ΔSR values for each PPI were compared to polyQ-dependent changes in interaction levels in 2m and 10m mice (Fig 4D & E). Paralleling polyQ length-dependent changes in its interaction levels, the vesicle-fusing ATPase, Nsf, also showed increased relative stability at both 2m and 10m. Two Htt PPIs that can directly interact with Nsf, syntaxin-1b (Stx1b) and synaptosomal-associated protein 25 (Snap25), were differently impacted by polyQ depending on age. Stx1b, which is involved in vesicle docking at presynaptic membranes, had a similar increase in interaction levels as Nsf, but only at 2m and showed no change in polyQ-dependent stability. In contrast, the interaction levels and relative stability of Snap25 was not influenced by polyQ under these conditions (Fig 4D–E).

To gain an integrative perspective of how PPI dynamics are impacted by polyQ, age, interaction level, and interaction stability, PPIs were assigned to one of eight classes (four primary classes and two sub-classes, Tables S4 and S5). The primary classes represent polyQ-dependent changes in interaction level only (Class 1), level and stability (Class 2), stability only (Class 3), or neither level or stability (Class 4) (Fig 4F, *right vs. left and outer vs. inner square*). Each primary class was divided into sub-classes “A” or “B”, based on whether the PPI showed (A) transient/decreasing or (B) stable/increasing dynamics. (Fig 4F, *top vs bottom*). Finally, PPIs within each of these classes were compared between 2m and 10m (Fig 4F, *Venn diagram*).

We observed that the majority of polyQ-dependent differential PPIs were not concurrently altered in their relative stability (Class 1). However, for PPIs with altered stability ratios, increases predominated over decreases (35 vs. 8 PPIs). Within the same interaction stability classes, there was less protein overlap (Fig 4F, *Venn intersection*) than would be predicted by the respective overlap of differential PPIs (42%, Fig 3C–D). This result suggests that

Author Manuscript Author Manuscript Author Manuscript Author Manuscript

mHtt-dependent differences in relative stability are less common than changes in levels, but the relative stability alterations are more often age-specific in HD mice.

Several functionally relevant Htt interacting partners belonged to different dynamic classes. For example, Hap40 and contactin1 (Cntn1) were stable interactions and not impacted by expanded polyQ, while catenin beta-1 (Ctnnb1) was one of the 30 PPIs that had increased interaction levels and became a more stable interaction with mHtt in at least one age (Fig 4D – E, and Fig 4F, c*lass 2B*). We also found that five subunits of the Arp2/3 protein complex (Actr2, Actr3, Actr3b, Arpc1a, and Arpc3), which regulates actin polymerization, were selectively increased in stability at the 2m but not 10m (Class 2B). In contrast, catenin alpha-1 (Ctnna1), a negative regulator of the Arp2/3 complex, which has not been previously identified as an Htt interactor, appears increased in stability at 10m. A small subset of PPIs had unchanged interaction levels but displayed altered stability (Fig 4F, Class 3), including the AP-2 complex subunit alpha-2 (Ap2a2), sodium/potassium-transporting ATPase subunit alpha-2 (Atp1a2), and voltage-dependent anion-selective channel protein 1 (Vdac1). Overall, the integration of metabolically labeled tissue as an internal reference to our IP-MS workflow allowed us to assess the impact of mHtt on PPI relative stability compared to interaction levels.

## PolyQ-dependent alterations in Htt PPI levels and stability occur within distinct protein networks of early and later stages of disease in HD mice

To identify cellular processes and pathways that may be impaired within striatal cells containing mHtt, we performed protein network and functional enrichment analysis for PPIs for which we had quantified interaction levels and stability. The majority of Htt PPI candidates (93%) were functionally interconnected, being linked to at least one other PPI in the STRING database. PPIs clustered into sub-networks enriched in specific functions (Fig S5A and Table S6). Htt was associated with a protein cluster involved in axonal transport, vesicle sorting processes and glutamate receptor signaling, eight of which are first neighbor STRING connections with Htt (Fig S5A, *red cluster and edges*). Within this cluster are AP2 adaptor complex subunits (Ap2a1, Ap2a2, Ap2b1) and six glutamate (AMPA and NDMA) receptor subunits (Gria1, Gria2, Gria3, Grin1, Grin2b, Grm3). Two other functionally related clusters contained proteins associated with the presynaptic zone (*dark green*) and establishment of axonal localization (*purple*). We next determined the relationship between PPI clusters and interaction dynamics by overlaying polyQ-dependent changes in relative stability at 2m and 10m (Fig 5). We found that stabilized PPIs at 2m (Fig 4F, Class 2B, and Table S5) were largely driven by proteins in the “regulation of actin cytoskeleton” functional cluster (Fig 5, *bright green*). This cluster included the previously mentioned Arp2/3 complex subunits, the F-actin-capping proteins (Capza1, Capza2, Capzb), as well as conventional (Myl6, Myh14, Myh9, Myh10) and non-conventional (Myo5a) myosins. We also identified stabilized interactions within the functional cluster containing connexin and catenin binding proteins (Fig 5, *orange*), while two subunits of the Na/K ATPase, ATPa1, α−1 and α−2, had opposite stability changes (Fig 5, *brown*). Notably, the majority of PPIs that had polyQ-dependent changes in stability at 2m were no longer impacted at 10m (Fig S4C, *top*). Two exceptions were Myl6, which showed a polyQ-dependent loss in stability at 10m, and beta-catenin (Ctnnb1), a first order neighbor Htt interaction that showed polyQ-dependent

Author Manuscript Author Manuscript Author Manuscript Author Manuscript

stabilization at 2 and 10m (Fig 5, *red asterisks* and Fig S4C, *bottom*). Overall, by placing relative stabilities within the context of clustered PPI networks, we discovered that PPIs with altered relative stabilities are predominantly found in the early versus later disease state of Q140 HD mouse pathogenesis and are largely associated with cytoskeletal structural components and their regulatory complexes.

## Mouse striatum HTT PPIs validated in a human HD cell model by bioluminescence-based two-hybrid assay

Our quantitative IP-MS assessment of PPI dynamics in mouse HD models uncovered 146 PPIs that are altered by interaction level, stability, or both, in at least one age (Table S4). To further validate these associations and assess their relevance in a human model system, we employed LuTHy, a double- readout luminescence- based two- hybrid assay (Trepte et al., 2018). We focused on 39 PPIs (Fig S5, *hexagonal nodes*) that were found within network “hotspots” (Fig 5) and ranked in the highest quartiles of IP/proteome abundance ratio (Fig S5B, *purple nodes*), supporting a greater enrichment with the bait (Tsai et al., 2012). Among the tested PPIs, 17 were differential based on polyQ-dependent interaction levels and stability and 22 were differential based on interaction levels alone. LuTHy evaluated the interaction potential of each putative PPI with HTTQ145 in human cells using *ex vivo* bioluminescence resonance energy transfer (BRET) and *in vitro* luminescence-based co-immunoprecipitation (LuC) assays. To allow for a double-readout in a single experiment, plasmids encoding nanoluciferase (NL)- and proteinA-mCitrine (PA-mCit)-tagged HTT interacting proteins (human orthologues) and full-length human mHTT were generated and each candidate PPI/HTTQ145 pair was expressed in all eight possible tagging combinations (Fig 6A–B). In-cell interaction was first assessed by BRET, which requires the NL donor and mCit acceptor interacting proteins to be in close proximity (<10 nm) (Wu and Brand, 1994). Then, the cell-free interaction was evaluated after cell lysis by LuC via immobilization of the PA-mCit-tagged protein and measurement of the NL signal of the co-isolated partner protein (Fig 6B). Of the 39 putative interacting proteins tested, 22 human orthologues were validated as interacting partners with human HTTQ145 in mammalian cells by LuTHy (Fig 6E, *LuTHy union*). Moreover, the LuTHy assay was not biased by PPI relative stability, as the SR distributions of the LuTHy-validated PPIs reflected the range of the entire set of HTT PPIs (Fig S6A vs. S4C). Overall, the LuTHy assay, with its dual readouts, provided increased confidence in the PPIs from mouse striatum and highlighted binary PPIs with a high probability of direct interaction.

## HTT protein interacting genes modulate mHTT-induced neuronal dysfunction in vivo

Our finding that the LuTHy assay detected a subset of the tested polyQ-dependent PPIs suggested that many of the PPIs identified in our IP-MS study may represent indirect associations with HTT. Moreover, these potential indirect associations are with proteins that have a range of functional classes (see Fig 5 and S5A), many of which have been linked to neuronal processes and therefore may support HTT’s roles at the synapse (Barron et al., 2021). To investigate the potential relevance of these PPIs to HD pathobiology, we selected ten genes encoding polyQ length-dependent PPIs to test for their ability to modulate mHTT-induced neuronal dysfunction. The ten PPIs were selected to represent different functional modules within the HTT interaction network (Fig 5), and included

Author Manuscript Author Manuscript Author Manuscript Author Manuscript

one PPI validated by LuTHy (ATP6V0D1) and one that was not confirmed (ATP6V1D) (Fig. 6). Since testing multiple genes in mice would be impractical, we took advantage of well-established *Drosophila* HD models (Onur et al., 2021; Romero et al., 2008). Specifically, fruit flies expressing either N-terminal or full-length mutant human HTT in neurons have been shown to display late-onset, progressive motor impairments that can be precisely measured by leveraging the *Drosophila* startle-induced negative geotaxis response (Al-Ramahi et al., 2018; Onur et al., 2021). Using this model, we performed a functional assay that quantitatively assesses neuronal dysfunction using motor performance metrics (i.e., speed; see Materials and Methods). Longitudinal data illustrated that *armadillo*, the *Drosophila* homologue of human CTNNB1, is a dosage-sensitive modifier of both full-length and N-terminal mutant human HTT (Fig 7A). The other nine *Drosophila* homologues of HTT PPI genes tested were found to be genetic modifiers that modulate (ameliorate or aggravate) full length mHTT-induced neuronal dysfunction as assessed in the longitudinal motor performance assay (Fig 7B). Notably, three of the tested HTT interacting proteins (CNTN1, ATP6V1D, and ATP6V0D1) have not been previously reported as genetic modifiers, while nine have not been previously found as genetic modifiers in the context of full length mHTT (Fig 7C). Interrogating our polyQ length-dependent PPIs more broadly, an additional 33 PPIs have been found as genetic modifiers of HD phenotypes in model systems ranging from yeast to mice (Table S7). Taken together, these results highlight the capability of our IP-MS approach to identify polyQ length-dependent PPIs that are also candidate genetic modifiers of Huntington's disease.

## Discussion

Characterization of PPIs has the potential to identify previously unrecognized biochemical activities of a target protein or provide insights into its roles in cellular pathways (Miteva et al., 2013; Szklarczyk et al., 2017). PPIs that are altered in a pathogenic state can be compensatory or disease drivers, providing clues into links to pathogenesis and targets for therapeutic agents (Lapek et al., 2017; Vanunu et al., 2010). While the accumulated knowledge of a large pool of potential HTT interacting partners has provided insights into its cellular functions (Harjes and Wanker, 2003; Saudou et al., 2016), assessment of connection to disease or therapeutic potential has remained limited. Here, we show that the mutant HTT forms protein interactions that are altered both in levels and relative stabilities, identifying high value polyQ-modulated and age-dependent PPIs that could be proximal to disease pathogenesis. Cross-validation of polyQ length-dependent PPIs with LuTHy two-hybrid assays and genetic modifier screening highlights the ability to accelerate prioritization of high value targets from larger interactomes. Our high congruence (>50%) between polyQ-dependent PPIs identified by IP-MS and validation by LuTHy in a human HD cell model suggests that a number of PPIs are direct interactions. Moreover, we found that both direct and indirect PPIs can modulate mHTT-induced neuronal dysfunction in *Drosophila* HD models. It is possible that PPI targets with shared properties of polyQ-dependence and annotation to cellular pathways with neuronal relevance inherently have higher probabilities of disease relevance. Future studies that continue to expand testing of PPIs as genetic disease modifiers will provide insights into the link between PPI dysregulation and HD pathobiology.

Author Manuscript Author Manuscript Author Manuscript Author Manuscript

An observation from our PPI study that mirrors previous reports is the association of HTT with proteins involved in vesicle targeting and fusion (Wanker et al., 2019). Our analysis highlighted that many of these PPIs are polyQ-dependent, including syntaxin-1B, vesicle-associated membrane protein 2 (VAMP2), SNAP25, NSF, and synapsins 1 and 2. SNARE proteins have been identified as interacting with HTT in multiple model systems (Culver et al., 2012; Ratovitski et al., 2012; Shirasaki et al., 2012; Zhao et al., 2018), and our study points to these proteins as perturbed PPIs at 2m. These early PPI changes may contribute to the known HD molecular phenotypes of impaired vesicle trafficking (Caviston and Holzbaur, 2009; Veldman and Yang, 2018) and synaptic function (Smith-Dijak et al., 2019), such as alterations in glutamatergic signaling (Fan and Raymond, 2007; McAdam et al., 2020; Metzler et al., 2007). Below we highlight selected high confidence PPIs that reflect these functions and how they relate to existing knowledge of HD pathobiology.

We found that the protein IQ Motif and Sec7 Domain ArfGEF 1 (IQSEC1) is a polyQ length-dependent and likely direct HTT interaction. IQSEC1 has previously been shown to modulate mHTT exon1 aggregation in HD model systems (Haenig et al., 2020). IQSEC1 is a guanine nucleotide exchange factor that activates ARF6, which can facilitate internalization of integrin receptors (Dunphy et al., 2006) and AMPA receptors in a long-term depression rat model (Scholz et al., 2010). Consistent with this, we found that the AMPA receptor subunit GLUR2 (GRIA2) is also modulated by polyQ and likely a direct HTT interaction. Other glutamate receptor subunits, GRIA1 and GRIA3 (AMPA receptor subunits), and GRIN1 and GRIN2B (NMDA receptor subunits) showed polyQ-dependent increases in interaction. The disease relevance of AMPA receptors is further supported by our finding that the *Drosophila* homologue of GRIA1/3 ameliorated motor performance deficits in flies expressing full length mHTT, consistent with a previous study in the context of N-terminal fragment mHTT (HTTN231Q128) (Al-Ramahi et al., 2018).

An open question regarding HD cellular pathobiology is: what is the mechanism of mHTT-dependent impairment of synaptic functions? One hypothesis supported by our results is that aberrant IQSEC1 interaction and/or function impacts glutamate receptor internalization. Previous studies have provided evidence for indirect involvement of HTT in clathrin-mediated receptor internalization (Metzler et al., 2003, 2007; Zhang et al., 2018). For example, NMDA-dependent AMPA receptor internalization was impaired in neurons lacking HTT interacting protein 1 (Metzler et al., 2003, 2007). More recently, in HD rodent models, hippocampal dysregulation of AMPA receptor trafficking was linked to defects in the BDNF-tyrosine receptor kinase B signaling pathway (Zhang et al., 2018), and mHTT-dependent alterations in receptor trafficking have been linked to changes in the synaptic distribution of glutamate-type receptors (Ambroziak et al., 2018; Zhang et al., 2018).

Our data also supports the possibility that mHTT-dependent impairment of vesicular trafficking could precede glutamate receptor dysregulation. For example, the increased interaction level and stability we observed between mHTT and NSF may impair the latter's ability to interact with GluR2, which could lead to decreased surface expression of AMPA receptors at the postsynaptic membrane (Noel et al., 1999). Impaired vesicular trafficking could also be relevant in the presynaptic terminals. McAdam and colleagues have observed a striatal-specific defect in synaptic vesicle endocytosis during high frequency

Author Manuscript Author Manuscript Author Manuscript Author Manuscript

stimulation of neurons isolated from 2m knock-in HD mice (McAdam et al., 2020). While the mechanism remains unclear, a mHTT-dependent defect in clathrin-mediated endocytosis has been observed in striatal cells (Borgonovo et al., 2013).

Another PPI functional class highlighted by our IP-MS study contained proteins that participate in actin cytoskeletal dynamics, for which we observed the largest consistent polyQ length-dependent increases in relative stability, occurring selectively at 2m (Fig 5, *green cluster*). Many cytoskeleton structural components are abundant cellular proteins and often are present as non-specific interactions in IP experiments. Yet, it is likely these PPIs are functionally relevant to HTT biology, as (1) HTT has a functional role in vesicular transport, which relies on the cytoskeletal network, (2) our study found they are perturbed by mHTT, and (3) these proteins had large IP enrichments (see Fig S5B).

PolyQ length-dependent dynamic PPIs in this functional cluster were components of known complexes, including the Arp2/3 complex, the CAPZalpha/beta heterodimer, and the SLC2A1-DMTN-ADD2 complex. The Arp2/3 complex is evolutionarily conserved and mediates actin filament assembly (Machesky et al., 1997; Welch et al., 1997). IP-MS analysis detected six out the nine complex subunits (ACTR2, ACTR3, ACTR3B, ARPC1A, ARPC2, and ARPC3). Based on our LuTHy analysis, ACTR2 and ACTR3B are probable direct HTT interacting partners, while ARPC1A and ARPC3 may be indirect. Except ARPC2, all of the other components had polyQ length-dependent changes in interaction level and stability.

The CAPZalpha/beta heterodimer binds growing ends of actin filaments and is also thought to be a peripheral component of the Wiskott-Aldrich syndrome protein and SCAR Homology (WASH) complex. The WASH complex governs endocytic vesicle fission in an Arp2/3-dependent manner and can inhibit CAPZ actin-capping activity (Jia et al., 2010). Intriguingly, a recent study from Courtland and colleagues found that a mouse model of a human mutation in WASH (WASHC4$^{c.3056C>G}$) causes defects in endosomal and lysosomal sorting, and phenotypically manifests as a cognitive-movement disorder in a mouse model and human patients (Courtland et al., 2021). It is tempting to speculate that mHTT remodeling of PPIs may impact WASH complex function and contribute to the pathobiological mechanisms contributing to the cognitive and motor deficits in HD.

Supporting the subcellular localization of HTT to the endosome, a collection of LuTHy-validated HTT PPIs were annotated as RHOBTB2 interactions at the endosomal membrane, represented by serine/threonine-protein kinase 38 (STK38), drebin (DBN1), and tropomodulins 1–3 (TMOD1, TMOD2, TMOD3) (Fig S6B). STK38 is a notable polyQ length-dependent PPI, being already altered at 2m in the Q140 HD mouse (Table S4), and potentially being deregulated at the gene level in striatal astrocytes and Drd1-positive medium spiny neurons ((Megret et al., 2021) and Table S7). Broadly, RHOBTB family members are atypical GTPases that participate in vesicle trafficking (Ji and Rivero, 2016) and in COP9 signalosome-regulated and CUL3-dependent protein ubiquitination (Berthold et al., 2008). Like HTT, the RHOBTB2 protein contains a proline-rich region. It is possible that these RHOBTB2-interacting proteins could also bind within the proline rich region of

Author Manuscript Author Manuscript Author Manuscript Author Manuscript

HTT. If mHTT sequesters proteins that normally interact with RHOBTB2, its function may be indirectly compromised.

Finally, our study found a mHTT-dependent, direct interaction with the V-type proton ATPase, as well as a previously unrecognized role in modulating HD pathogenesis. V-ATPase is a multi-subunit enzyme that functions to acidify intracellular organelles, being comprised of an integral membrane complex that translocate protons (V0) and a soluble complex that hydrolyzes ATP (V1) (Wilkens et al., 2004). Interestingly, subunits belonging to V0 and V1 showed opposing effects in modulating mHTT-induced toxicity in our *Drosophila* behavioral assays. Knockdown of the three V1 subunits (ATP6V1A, ATP6V1D, ATP6V1E1) showed amelioration, while knockdown of the V0 subunit (ATP6V0D1) exacerbated mHTT-induced motor performance. A mechanistic link between V-ATPase activity and the pathobiology of Huntington's disease has not been shown. However, lysosomal acidification by V-ATPase is necessary for autophagy, which is known to be impaired in several HD model systems (Martin et al., 2015), specifically through disruptions in autophagosome trafficking (Wong and Holzbaur, 2014) and cargo loading (Martinez-Vicente et al., 2010).

Overall, our study leveraged complementary and orthogonal protein interactions approaches and HD model systems to assemble candidates of Huntington's disease modifiers and provide a resource for future studies on the cellular biology of HTT. The identification of mutant HTT-induced alterations in interactions with proteins that are also genetic disease modifiers can contribute to the assembly of pathway-based models of disease progression (Megret et al., 2021). Our data suggest an HD model in which, prior to striatal cell death, mHTT sequesters signaling proteins and enzymatic regulators that control synapse morphology and neurotransmission. The continued aberrant association of these PPIs contributes to further interactome remodeling, changing associations with components at pre-synaptic sites of vesicle release/recycling and postsynaptic densities.

## STAR Methods

### LEAD CONTACT AND MATERIALS AVAILABILITY

Further information and requests for resources and reagents should be directed to and will be fulfilled by the Lead Contact, Ileana M. Cristea (icristea@princeton.edu).

**Materials availability—**This study did not generate new unique reagents.

### Data and Code Availability

- The mass spectrometry proteomics data have been deposited at ProteomeXchange Consortium via the PRIDE (Perez-Riverol et al., 2019) partner repository and are publicly available as of the date of publication. Accession numbers are listed in the key resources table. Data generated by the Drosophila motor performance assay will be shared by the lead contact upon request.
- This paper does not report original code.

Author Manuscript Author Manuscript Author Manuscript Author Manuscript

- Any additional information required to reanalyze the data reported in this paper is available from the lead contact upon request

## EXPERIMENTAL MODEL AND SUBJECT DETAILS

### Animals

**Mouse strains:** The huntingtin N-terminal Flag-tagged control (*Htt*$^{3xFlagQ20/+}$) and HD knock-in (*Htt*$^{3xFlagQ140/+}$) male and female mice are congenic in the C57BL/6J background. Mice were housed in a humidity- and temperature-controlled room with 12-hour light-dark schedule. Food and water were provided ad libitum. All experimental procedures were performed in accordance with UVA Institutional Animal Care and Use guidelines, and precautions were taken to minimize stress and the number of animals used. UVA is fully accredited by AALAC, and the University has a PHS Assurance on file with the Office of Laboratory Animal Welfare (PHS Assurance # A33245–01).

**Drosophila strains:** *Drosophila* strains carrying *UAS*-HTT$^{FL[Q200]}$ and *UAS*-HTT$^{NT231[Q128]}$ have been previously characterized (Onur et al., 2021; Romero et al., 2008). Pan-neuronal expression was achieved using the *elav-GAL4*(C155) driver from BDSC (Bloomington Drosophila Stock Center). The alleles tested were obtained from the BDSC and from the Vienna Drosophila Resource Center (VDRC). *Drosophila* homologs were identified using Blast and also the DRSC Integrative Ortholog Prediction Tool (Hu et al., 2011). Genotypes used are summarized in Table S9.

### Cell lines

**Human embryonic kidney cell line 293 (HEK293) cultures:** HEK293 cells were cultured in high glucose (4.5 g/L) media supplemented with 10% heat inactivated fetal bovine serum (Gibco®, ThermoFisher) and grown at 37°C and 5% $CO_2$.

## METHOD DETAILS

**Mouse tissue harvesting—**Brains were harvested from male and female 2- and 10-month-old mice following isoflurane anesthesia and cervical dislocation. Brains were cut in half sagittally, and immediately frozen in 2-Methylbutane (Fisher Scientific O3551–4) pre-equilibrated in dry ice. Striata were isolated in a petri dish on ice and placed immediately in 1.5 ml tubes pre-chilled in dry ice. Tissues that were used in paired control and experimental immunoaffinity purifications within the same biological replicate were sex-matched.

**Western blot analysis:** Protein samples from immunoisolations (input, pellet, flow-through, and elution) were loaded onto 4–12% Bis-Tris gels (Thermo Fisher Scientific, Waltham. MA) and separated for 10 min at 100V, then for 70 min at constant current of 70 amps. Proteins were transferred onto PVDF membranes (Immobilon-FL, MilliporeSigma) overnight at a constant 40V. Membranes were blocked in Tris-buffered saline (TBS) containing 5% milk for one hour at room temperature, then incubated with mouse anti-FLAG (Sigma, F3165, 1.0 μg / mL) antibody in blocking buffer with 0.1% tween-20 (TBSt) for 90 min at room temperature. Membranes were washed 4 × 5 min with TBSt, then incubated with goat anti-mouse Alexa Fluor 680 secondary antibody (A-21058,

Author Manuscript Author Manuscript Author Manuscript Author Manuscript

ThermoFisher Scientific) diluted 1:10,000 in TBSt containing 5% milk for 45 min at room temperature. Membranes were imaged on the LI-COR Odyssey CLx system (LI-COR Biosciences, Lincoln, NE) using automatic settings.

**Preparation of Protein A/G beads coated with FLAG antibody and immunoaffinity purification of 3xFLAG-Htt:** Magnetic Protein A/G beads (Thermo Scientific, PI-88802) were freshly pre-coupled to either non-specific mouse IgG or anti-FLAG M2 antibody (Sigma, F1804). Briefly, 60 µL of protein A/G slurry was washed with 3 × 500 µL of 20 mM K-HEPES pH 7.4, containing 110 mM KOAc, 2 mM $MgCl_2$, 0.1% Tween-20, 1 µM $ZnCl_2$, 1 µM $CaCl_2$, 150 mM NaCl, then resuspended in fresh wash buffer and split into 2 × 500 µL aliquots. One aliquot was mixed with 12 µL of 1 µg/µL anti-FLAG M2 antibody, and the other with 1.2 µL of 10 µg/µL mouse IgG. Bead-antibody mixtures were incubated for 1 hour at 4C under rotation, then washed with 2 × 500 µL wash buffer, resuspended in 40 µL of wash buffer, and used for immunoaffinity purifications.

Immunoaffinity purifications were performed from protein lysates extracted from either whole mouse brains or pooled striata. For label-free IP-MS, the equivalent of ½ of a brain hemisphere or 3 dissected striata were used per IP. Briefly, brain tissues were minced in a small volume of lysis buffer (20 mM K-HEPES pH 7.4, 110 mM KOAc, 2 mM $MgCl_2$, 0.1% Tween-20, 1 µM $ZnCl_2$, 1 µM $CaCl_2$, 150 mM NaCl, and 1% Triton-X100 supplemented with Halt protease and phosphatase inhibitors and Universal nuclease (Thermo Scientific)) on wet ice and homogenized with 20 strokes on wet ice in either 4 mL of lysis buffer in a Tenbroeck tissue grinder (whole brain) or 2 mL of lysis buffer in a Potter-Elvehjem tissue grinder (striata). The homogenized tissue was transferred to a conical tube containing an equivalent volume of lysis buffer, then incubated on wet ice for 5 min, and centrifuged at 8000 × g for 10 min at 4 °C. Soluble proteins were recovered and the protein yield was measured by the BCA assay (Thermo Fisher Scientific, 23225). Immunoisolation of whole brain and striatum were performed with ~7 mg of input protein, which was equally applied to Protein A/G beads coated with anti-FLAG or non-specific IgG antibodies (see above) and incubated at 4 °C for 1 hr under rotation.

Protein A/G beads containing bound protein complexes were collected against a magnetic, suspended in 0.5 mL of IP wash buffer (lysis buffer lacking protease and phosphatase inhibitors), and transferred to a fresh 2 mL round bottom tube. The beads were washed sequentially with 3 × 0.5 mL of IP wash buffer, 1 × 0.5 mL of cold $ddH_2O$ and transferred to a fresh round bottom tube, and 1 × 0.5 mL of cold $ddH_2O$. Proteins were eluted and magnetically separated from the washed beads in 50 µL of 106 mM Tris HCl, 141 mM Tris base, 2% LDS, 0.5 mM EDTA at 70 °C for 10 min. Note, as the IP lysis buffer was designed to maintain weaker and/or transient interactions, the captured proteins largely reflect associations with Triton-soluble forms mHtt (Ochaba et al., 2018), either as full-length or N-terminal fragments. The eluted proteins were mixed with 25 mM TCEP (Thermo Fisher Scientific, 20491) and 50 mM chloroacetamide and incubated at 70 °C for 20 min. Proteins were then digested in-solution with trypsin using filter aided sample preparation (Erde et al., 2014; Manza et al., 2005; Wiśniewski et al., 2009) and the resulting peptides were separated into three fractions by SDB-RPS StageTips (Kulak et al., 2014) as previously described (Greco et al., 2016).

Author Manuscript Author Manuscript Author Manuscript Author Manuscript

**Metabolic labeling immunoaffinity purification of 3xFLAG-Htt:** $^{13}C_6$-lysine (97% enriched)-labeled mouse whole brain tissues (2m and 10m, MT-LYSC6-MB-PK, Cambridge Isotopes) were used for metabolic labeled IP-MS as labeled striatal tissues were not practical to obtain in sufficient quantity. Prior to their use in metabolic labeling IP-MS, the extent of $^{13}C$ protein enrichment was verified by whole proteome analysis. Briefly, aliquots of tissue were lysed using sonication and heat (97°C) in 50 mM HEPES, pH 8.2, 100 mM NaCl, 0.5 mM EDTA, 4% SDS, and treated for 5 min at 97°C with 10 mM TCEP, then 20 min at 70°C with 40 mM chloroacetamide. A methanol-chloroform precipitation was performed to remove detergents and low molecular weight contaminants. Precipitated pellets were resuspended in 25mM HEPES, pH 8.2, at 0.5 μg/μL, and digested overnight with trypsin at 37°C in a Thermomixer with gentle agitation. Peptides were desalted by $C_{18}$ StageTips and analyzed by 1D-nanoLC-MS/MS, as described below.

Immunoaffinity purification of 3xFLAG-Htt in metabolic labeled IP-MS experiments were performed similar to the label-free IP-MS experiments, except the equivalent of 2.5 striata were used per IP and were mixed with an equal protein amount (w:w) of age-matched, $^{13}C_6$-lysine labeled brain lysate extracted from whole brain.

**LC-MS/MS analysis:** Digested and fractionated IP eluates were analyzed on an Ultimate 3000 nanoRSLC coupled online with an ESI-LTQ-Orbitrap Velos ETD mass spectrometer (Thermo Electron, San Jose, CA) as previously described (Federspiel et al., 2019). Reverse-phase chromatography was performed over a 20 cm IntegraFrit column (IF360-75-50-N-5, New Objective, Woburn, MA) packed in-house with 1.9 μm ReproSil-Pur C18-AQ (Dr. Maisch, GmbH) with mobile phase A: 0.1% formic acid in water and mobile phase B: 0.1% formic acid in 97% acetonitrile. Peptides were separated over a 150 min (label-free) or 180 min (isotope-labeled) gradient (5% B to 30% B) with 250 nL/min flow rate and detected by a precursor scan followed by data-dependent collision-induced dissociation (CID) MS/MS fragmentation of top 15 most abundant ions. The following parameters were used: FT preview scan disabled, waveform injection and dynamic exclusion enabled, automatic gain control target value of $1 \times 10^6$ for MS and $1 \times 10^4$ for ion trap MS/MS scans, max ion injection time of 300 ms for MS and 125 ms for MS/MS scans. For MS scans: *m/z* range of 350–1,700 and resolution of 120,000; for MS/MS scans: minimum signal of 1,000, isolation width of 2.0, normalized collision energy of 30% and activation time of 10 ms.

**Informatics analysis of protein interaction specificity:** MS/MS spectra were searched against a FASTA file containing mouse protein sequences and common contaminants (16,932 sequences, download 7/2016 from Uniprot) using Proteome Discoverer 2.2.0.388. The Spectrum Files RC node and Minora Feature Detector nodes were used to perform offline mass recalibration and label-free MS1 quantitation, respectively. The data were searched using SequestHT with the following parameters: Full trypsin enzyme specificity, a maximum of two missed cleavages, precursor mass tolerance of 5 ppm, fragment mass tolerance of 0.3 Da, static carbamidomethylation of cysteine, dynamic oxidation of methionine, dynamic deamidation of asparagine, dynamic loss of methionine plus acetylation of the protein N-terminus, and dynamic phosphorylation of serine, threonine, and tyrosine. A reverse database search was performed, which was used to control FDR to 1% at

Author Manuscript Author Manuscript Author Manuscript Author Manuscript

the spectra, peptide, and protein levels. The forward and reverse peptide spectrum matches were then analyzed by the Percolator node to assign q-values. FLAG and control IP datasets were assembled into a consensus file using the default workflow (Proteome Discoverer 2.2), but with Feature Mapper and Precursor Ions Quantifier nodes. The assembled protein identifications with associated spectral counts were exported to Excel and analyzed by SAINT (Choi et al., 2011) integrated within the Resource for Evaluation of Protein Interaction Networks (REPRINT) server (https://reprint-apms.org/?q=reprint-home) for PPI specificity scoring. Spectral counts were utilized for SAINT scoring as they are well-suited for detecting large abundance differences between samples that are typically observed in IP enrichment experiments. To account for sampling variances between replicates across FLAG and control IPs, individual protein spectral counts were normalized by the total spectral counts. The interaction probability of each co-isolated protein was scored using normalized protein spectral counting data from FLAG-Htt and control IPs in each of the four conditions (Q20–2m, Q140–2m, Q20–10m, and Q140–10m). SAINT was run with LowMode “disabled” and MinFold and Normalize “enabled”. The average SAINT score from the best two replicates in each condition was used for specificity assessment.

**Label-free and isotope-labeled quantification of HTT interactions:** For differential interactions and normalization of PPI abundances, a consensus report was assembled in Proteome Discoverer 2.2 combining each FLAG IP dataset. The MSF file node was set to merge experiments “per file and search engine type”. The false discovery rate (FDR) (Strict) settings in the Peptide Validator node were set to 0.01. The feature matching strategy of the $MS^1$-based label-free quantification was enabled, which improved the consistency of detection by using peptides supported by MS/MS sequencing in at least one IP to establish their presence in other samples (Zhu et al., 2010). The maximum peak intensity for each peptide was determined and used to calculated peptide ratio-based and summed protein abundances. For label-free experiments, prey abundances were normalized to the respective bait (Htt) abundance. Normalized protein abundances were required to have ≥ two identified unique peptide sequences and ≥ two quantified unique+razor peptides.

**Bioinformatics analysis of HTT interactions:** Network interaction diagrams incorporating relative quantitation and known protein-protein interaction data were generated in Cytoscape (Shannon et al., 2003) using information and enrichments from STRING (Szklarczyk et al., 2019). The ClueGO app (Bindea et al., 2009) in Cytoscape was used to perform different sets of two-group comparisons of enriched proteins and interactions. Heatmaps of the quantitative MS1 data were generated using Morpheus (Broad Institute, https://software.broadinstitute.org/morpheus). Principal component analysis (PCA) was conducted using the Clustvis (Metsalu and Vilo, 2015) web tool. Overrepresentation analysis was performed against the Reactome pathway database (Fabregat et al., 2018) through the Panther (Mi et al., 2017) web interface (http://pantherdb.org). Previously identified HTT-interacting proteins and striatal disease signature datasets were obtained from the HDinHD data portal (Aaronson et al., 2021). Parts of some figures were generated using https://biorender.io under an academic license.

Author Manuscript Author Manuscript Author Manuscript Author Manuscript

**Targeted validation of HTT interactions with LuTHy:** LuTHy screens were performed as described in Trepte et al. (2018). In brief, open reading frames of candidate human HTT interactors and full-length human HTT with an expanded polyglutamine region (HTTQ145) were cloned in LuTHy expression vectors (Table S8) by standard linear recombination reactions using the Gateway Cloning System and validated by restriction enzyme digest, agarose gel electrophoresis, and Sanger sequencing. Interaction pairs were tested in all possible 8 orientations: N/C-terminal tagging with Nanoluciferase (NL)/Protein A-mCitrine (PA-mCit). LuTHy control vectors expressing only NL or PA-mCit were used for calculation of corrected scores. HEK293 cells were reverse transfected using linear polyethyleneimine (25 kDa, Polysciences 23966) with LuTHy constructs and cells were subsequently incubated for 48 h. In-cell BRET measurements were carried out in flat-bottom white 96-well plates (Greiner, 655983) with 24 PPIs per plate (each PPI in triplicate). For cell-free LuC measurements, cells in 96-well plates were lysed and lysates were transferred to 384-well plates resulting in 96 PPIs per plate (Greiner, 784074). Infinite® microplate readers M200, M1000, or M1000Pro (Tecan) were used for the readouts with the following settings: fluorescence of mCitrine recorded at Ex 500 nm/Em 530 nm, luminescence measured using blue (370–480 nm) and green (520–570 nm) band pass filters with 1,000 ms (LuTHy-BRET) or 200 ms (LuTHy-LuC) integration time. A PPI was considered positive if its corrected BRET (cBRET) or LuC (cLuC) ratio was ≥0.01 and ≥0.03, respectively (Fig 6C & D) (Trepte et al., 2018).

***Drosophila* Motor Performance Assay:** For the motor performance tests, we used a highly automated behavioral assay based on the *Drosophila* startle-induced negative geotaxis response as previously described (Onur et al., 2021). To assess motor performance of fruit flies as a function of age, we used ten age-matched virgin females per replica per genotype. Flies were collected in a 24hr period and transferred to new vials containing 300µl of media every day. Four replicates were used per genotype. Using an automated platform, the animals were taped to the bottom of a plastic vial and video-recorded for 7.5 seconds. Videos were analyzed using custom software to assess the speed of each individual animal. Three trials per replicate were performed each day shown, and four replicates per genotype are used. A linear mixed effect model ANOVA was run using each four replicates to assess statistical significance across genotypes.

## QUANTIFICATION AND STATISTICAL ANALYSIS

Statistical analyses were performed in Graphpad Prism 9 or Microsoft Excel as described below. P-values for polyQ-dependent changes in IP-MS protein abundances (Q140 vs Q20) were determined by unpaired t-test (mean ± SD, n =3, *p < 0.05). For analysis of differences between heatmap cluster means (Figure 2B), a non-parametric Kruskal-Wallis test, followed by a Dunn's multiple comparison post-test was used to determine statistical significance of Q140 versus Q20 for 2m and 10m sample groups (n = number of proteins within each cluster, see heatmap in Fig 2A; *, p < 0.05; ***, p < 0.001; ****, p < 0.0001). In Drosophila motor performance assays, the effect of genetic modifiers was evaluated following mixed models ANOVA (mean ± SEM, * p<0.05, ** p<0.01, *** p<0.001). Additional details are provided in the figure legends.

Author Manuscript Author Manuscript Author Manuscript Author Manuscript

## Supplementary Material

Refer to Web version on PubMed Central for supplementary material.

## Acknowledgements

We would like to thank Thomas Vogt, Daniel Lavery, Ravi Iyer, Brinda Prasad, and the investigators of the CHDI PPI working group for thoughtful discussions about experimental design and data interpretation. IMC and EW are grateful for funding from the CHDI Foundation, USA, EW is supported by the Helmholtz Association (iMed and Helmholtz-Israel Initiative on Personalized Medicine, Germany). SOZ and J-PL are supported by NIH NS077926 and NS090914. JB is supported by AG/NIA/NIH R01 AG057339.

## References

Aaronson J, Beaumont V, Blevins RA, Andreeva V, Murasheva I, Shneyderman A, Armah K, Gill R, Chen J, Rosinski J, et al. (2021). HDinHD: A Rich Data Portal for Huntington's Disease Research. J. Huntingtons. Dis 10, 405–412. [PubMed: 34397420]

Al-Ramahi I, Lu B, Di Paola S, Pang K, de Haro M, Peluso I, Gallego-Flores T, Malik NT, Erikson K, Bleiberg BA, et al. (2018). High-Throughput Functional Analysis Distinguishes Pathogenic, Nonpathogenic, and Compensatory Transcriptional Changes in Neurodegeneration. Cell Syst 7, 28–40.e4. [PubMed: 29936182]

Ambroziak W, Fourie C, and Montgomery JM (2018). SAP97-mediated rescue of NMDA receptor surface distribution in a neuronal model of Huntington's disease. Hippocampus 28, 707–723. [PubMed: 30067285]

Antonicka H, Lin ZY, Janer A, Aaltonen MJ, Weraarpachai W, Gingras AC, and Shoubridge EA (2020). A High-Density Human Mitochondrial Proximity Interaction Network. Cell Metab 32, 479–497.e9. [PubMed: 32877691]

Ast A, Buntru A, Schindler F, Hasenkopf R, Schulz A, Brusendorf L, Klockmeier K, Grelle G, McMahon B, Niederlechner H, et al. (2018). mHTT Seeding Activity: A Marker of Disease Progression and Neurotoxicity in Models of Huntington's Disease. Mol. Cell 71, 675–688.e6. [PubMed: 30193095]

Banks CAS, Zhang Y, Miah S, Hao Y, Adams MK, Wen Z, Thornton JL, Florens L, and Washburn MP (2020). Integrative Modeling of a Sin3/HDAC Complex Sub-structure. Cell Rep 31.

Barron JC, Hurley EP, and Parsons MP (2021). Huntingtin and the Synapse. Front. Cell. Neurosci 15.

Bates GP, Dorsey R, Gusella JF, Hayden MR, Kay C, Leavitt BR, Nance M, Ross CA, Scahill RI, Wetzel R, et al. (2015). Huntington disease. Nat. Rev. Dis. Prim 1.

Bergendahl LT, Gerasimavicius L, Miles J, Macdonald L, Wells JN, Welburn JPI, and Marsh JA (2019). The role of protein complexes in human genetic disease. Protein Sci 28, 1400–1411. [PubMed: 31219644]

Berthold J, Schenková K, and Rivero F (2008). Rho GTPases of the RhoBTB subfamily and tumorigenesis. Acta Pharmacol. Sin 29, 285–295. [PubMed: 18298893]

Bindea G, Mlecnik B, Hackl H, Charoentong P, Tosolini M, Kirilovsky A, Fridman WH, Pagès F, Trajanoski Z, and Galon J (2009). ClueGO: A Cytoscape plug-in to decipher functionally grouped gene ontology and pathway annotation networks. Bioinformatics 25, 1091–1093. [PubMed: 19237447]

Borgonovo JE, Troncoso M, Lucas JJ, and Sosa MA (2013). Mutant huntingtin affects endocytosis in striatal cells by altering the binding of AP-2 to membranes. Exp. Neurol 241, 75–83. [PubMed: 23219902]

Budayeva HG, and Cristea IM (2014). A mass spectrometry view of stable and transient protein interactions. Adv Exp Med Biol 806, 263–282. [PubMed: 24952186]

Carroll JB, Bates GP, Steffan J, Saft C, and Tabrizi SJ (2015). Treating the whole body in Huntington's disease. Lancet Neurol 14, 1135–1142. [PubMed: 26466780]

Caviston JP, and Holzbaur ELF (2009). Huntingtin as an essential integrator of intracellular vesicular trafficking. Trends Cell Biol 19, 147–155. [PubMed: 19269181]

Author Manuscript Author Manuscript Author Manuscript Author Manuscript

Choi H, and Nesvizhskii AI (2008). Semisupervised model-based validation of peptide identifications in mass spectrometry-based proteomics. J. Proteome Res 7, 254–265. [PubMed: 18159924]

Choi H, Larsen B, Lin ZY, Breitkreutz A, Mellacheruvu D, Fermin D, Qin ZS, Tyers M, Gingras AC, and Nesvizhskii AI (2011). SAINT: probabilistic scoring of affinity purification-mass spectrometry data. Nat. Methods 8, 70–73. [PubMed: 21131968]

Ciarochi JA, Johnson HJ, Calhoun VD, Liu J, Espinoza FA, Bockholt HJ, Misiura M, Caprihan A, Plis S, Paulsen JS, et al. (2019). Concurrent Cross-Sectional and Longitudinal Analyses of Multivariate White Matter Profiles and Clinical Functioning in Pre-Diagnosis Huntington Disease. J. Huntingtons. Dis 8, 199–219. [PubMed: 30932891]

Courtland JL, Bradshaw TWA, Waitt G, Soderblom EJ, Ho T, Rajab A, Vancini R, Kim IH, and Soderling SH (2021). Genetic disruption of washc4 drives endo-lysosomal dysfunction and cognitive-movement impairments in mice and humans. Elife 10.

Culver BP, Savas JN, Park SK, Choi JH, Zheng S, Zeitlin SO, Yates JR 3rd, Tanese N, Yates JR, and Tanese N (2012). Proteomic analysis of wild-type and mutant huntingtin-associated proteins in mouse brains identifies unique interactions and involvement in protein synthesis. J Biol Chem 287, 21599–21614. [PubMed: 22556411]

DiFiglia M, Sapp E, Chase KO, Davies SW, Bates GP, Vonsattel JP, and Aronin N (1997). Aggregation of huntingtin in neuronal intranuclear inclusions and dystrophic neurites in brain. Science (80-.) 277, 1990–1993.

Dunphy JL, Moravec R, Ly K, Lasell TK, Melancon P, and Casanova JE (2006). The Arf6 GEF GEP100/BRAG2 regulates cell adhesion by controlling endocytosis of β1 integrins. Curr. Biol 16, 315–320. [PubMed: 16461286]

Erde J, Loo RRO, and Loo JA (2014). Enhanced FASP (eFASP) to increase proteome coverage and sample recovery for quantitative proteomic experiments. J. Proteome Res 13, 1885–1895. [PubMed: 24552128]

Fan MMY, and Raymond LA (2007). N-Methyl-d-aspartate (NMDA) receptor function and excitotoxicity in Huntington's disease. Prog. Neurobiol 81, 272–293. [PubMed: 17188796]

Federspiel JD, Greco TM, Lum KK, and Cristea IM (2019). Hdac4 interactions in huntington's disease viewed through the prism of multiomics. Mol. Cell. Proteomics 18, S92–S113. [PubMed: 31040226]

Gao R, Chakraborty A, Geater C, Pradhan S, Gordon KL, Snowden J, Yuan S, Dickey AS, Choudhary S, Ashizawa T, et al. (2019). Mutant huntingtin impairs PNKP and ATXN3, disrupting DNA repair and transcription. Elife 8.

Goehler H, Lalowski M, Stelzl U, Waelter S, Stroedicke M, Worm U, Droege A, Lindenberg KS, Knoblich M, Haenig C, et al. (2004). A protein interaction network links GIT1, an enhancer of huntingtin aggregation, to Huntington's disease. Mol. Cell 15, 853–865. [PubMed: 15383276]

Greco TM, Guise AJ, and Cristea IM (2016). Determining the composition and stability of protein complexes using an integrated label-free and stable isotope labeling strategy (Humana Press Inc.).

Guo Q, Huang B, Cheng J, Seefelder M, Engler T, Pfeifer G, Oeckl P, Otto M, Moser F, Maurer M, et al. (2018). The cryo-electron microscopy structure of huntingtin. Nature 555, 117–120. [PubMed: 29466333]

Haenig C, Atias N, Taylor AK, Mazza A, Schaefer MH, Russ J, Riechers SP, Jain S, Coughlin M, Fontaine JF, et al. (2020). Interactome Mapping Provides a Network of Neurodegenerative Disease Proteins and Uncovers Widespread Protein Aggregation in Affected Brains. Cell Rep 32.

Harding RJ, Loppnau P, Ackloo S, Lemak A, Hutchinson A, Hunt B, Holehouse AS, Ho JC, Fan L, Toledo-Sherman L, et al. (2019). Design and characterization of mutant and wildtype huntingtin proteins produced from a toolkit of scalable eukaryotic expression systems. J. Biol. Chem 294, 6986–7001. [PubMed: 30842263]

Harjes P, and Wanker EE (2003). The hunt for huntingtin function: Interaction partners tell many different stories. Trends Biochem. Sci 28, 425–433. [PubMed: 12932731]

Hashimoto Y, Sheng X, Murray-Nerger LA, and Cristea IM (2020). Temporal dynamics of protein complex formation and dissociation during human cytomegalovirus infection. Nat. Commun *11*.

Author Manuscript Author Manuscript Author Manuscript Author Manuscript

Hickey MA, Kosmalska A, Enayati J, Cohen R, Zeitlin S, Levine MS, and Chesselet MF (2008). Extensive early motor and non-motor behavioral deficits are followed by striatal neuronal loss in knock-in Huntington's disease mice. Neuroscience 157, 280–295. [PubMed: 18805465]

Hodgson JG, Agopyan N, Gutekunst CA, Leavitt BR, Lepiane F, Singaraja R, Smith DJ, Bissada N, McCutcheon K, Nasir J, et al. (1999). A YAC mouse model for Huntington's disease with full-length mutant huntingtin, cytoplasmic toxicity, and selective striatal neurodegeneration. Neuron 23, 181–192. [PubMed: 10402204]

Hu Y, Flockhart I, Vinayagam A, Bergwitz C, Berger B, Perrimon N, and Mohr SE (2011). An integrative approach to ortholog prediction for disease-focused and other functional studies. BMC Bioinformatics 12.

Jean Beltran PM, Federspiel JD, Sheng X, and Cristea IM (2017). Proteomics and integrative omic approaches for understanding host–pathogen interactions and infectious diseases. Mol. Syst. Biol 13, 922. [PubMed: 28348067]

Ji W, and Rivero F (2016). Atypical Rho GTPases of the RhoBTB Subfamily: Roles in Vesicle Trafficking and Tumorigenesis. Cells 5, 28.

Jia D, Gomez TS, Metlagel Z, Umetani J, Otwinowski Z, Rosen MK, and Billadeau DD (2010). WASH and WAVE actin regulators of the Wiskott-Aldrich syndrome protein (WASP) family are controlled by analogous structurally related complexes. Proc. Natl. Acad. Sci. U. S. A 107, 10442–10447. [PubMed: 20498093]

Joshi P, Greco TM, Guise AJ, Luo Y, Yu F, Nesvizhskii AI, and Cristea IM (2013). The functional interactome landscape of the human histone deacetylase family. Mol Syst Biol 9, 672. [PubMed: 23752268]

Kaltenbach LS, Romero E, Becklin RR, Chettier R, Bell R, Phansalkar A, Strand A, Torcassi C, Savage J, Hurlburt A, et al. (2007). Huntingtin interacting proteins are genetic modifiers of neurodegeneration. PLoS Genet 3, e82. [PubMed: 17500595]

Kim YE, Hosp F, Frottin F, Ge H, Mann M, Hayer-Hartl M, and Hartl FU (2016). Soluble Oligomers of PolyQ-Expanded Huntingtin Target a Multiplicity of Key Cellular Factors. Mol. Cell 63, 951–964. [PubMed: 27570076]

Kulak NA, Pichler G, Paron I, Nagaraj N, and Mann M (2014). Minimal, encapsulated proteomic-sample processing applied to copy-number estimation in eukaryotic cells. Nat. Methods 11, 319–324. [PubMed: 24487582]

Langfelder P, Cantle JP, Chatzopoulou D, Wang N, Gao F, Al-Ramahi I, Lu XH, Ramos EM, El-Zein K, Zhao Y, et al. (2016). Integrated genomics and proteomics define huntingtin CAG length-dependent networks in mice. Nat. Neurosci 19, 623–633. [PubMed: 26900923]

Lapek JD, Greninger P, Morris R, Amzallag A, Pruteanu-Malinici I, Benes CH, and Haas W (2017). Detection of dysregulated protein-association networks by high-throughput proteomics predicts cancer vulnerabilities. Nat. Biotechnol 35, 983–989. [PubMed: 28892078]

Liu Z, Gong Z, Dong X, and Tang C (2016). Transient protein-protein interactions visualized by solution NMR. Biochim. Biophys. Acta - Proteins Proteomics 1864, 115–122.

MacDonald ME, and Gusella JF (1996). Huntington's disease: Translating a CAG repeat into a pathogenic mechanism. Curr. Opin. Neurobiol 6, 638–643. [PubMed: 8937828]

MacDonald ME, Ambrose CM, Duyao MP, Myers RH, Lin C, Srinidhi L, Barnes G, Taylor SA, James M, Groot N, et al. (1993). A novel gene containing a trinucleotide repeat that is expanded and unstable on Huntington's disease chromosomes. Cell 72, 971–983. [PubMed: 8458085]

Machesky LM, Reeves E, Wientjes F, Mattheyse FJ, Grogan A, Totty NF, Burlingame AL, Hsuan JJ, and Segal AW (1997). Mammalian actin-related protein 2/3 complex localizes to regions of lamellipodial protrusion and is composed of evolutionarily conserved proteins. Biochem. J 328, 105–112. [PubMed: 9359840]

Maiuri T, Bowie LE, and Truant R (2019). DNA Repair signaling of huntingtin: The next link between late-onset neurodegenerative disease and oxidative DNA damage. DNA Cell Biol 38, 1–6. [PubMed: 30481056]

Manza LL, Stamer SL, Ham AJL, Codreanu SG, and Liebler DC (2005). Sample preparation and digestion for proteomic analyses using spin filters. Proteomics 5, 1742–1745. [PubMed: 15761957]

Author Manuscript Author Manuscript Author Manuscript Author Manuscript

Martin DDO, Ladha S, Ehrnhoefer DE, and Hayden MR (2015). Autophagy in Huntington disease and huntingtin in autophagy. Trends Neurosci 38, 26–35. [PubMed: 25282404]

Martinez-Vicente M, Talloczy Z, Wong E, Tang G, Koga H, Kaushik S, De Vries R, Arias E, Harris S, Sulzer D, et al. (2010). Cargo recognition failure is responsible for inefficient autophagy in Huntington's disease. Nat. Neurosci 2010 135 13, 567–576. [PubMed: 20383138]

McAdam RL, Morton A, Gordon SL, Alterman JF, Khvorova A, Cousin MA, and Smillie KJ (2020). Loss of huntingtin function slows synaptic vesicle endocytosis in striatal neurons from the httQ140/Q140 mouse model of Huntington's disease. Neurobiol. Dis 134.

Megret L, Gris B, Nair SS, Cevost J, Wertz M, Aaronson J, Rosinski J, Vogt TF, Wilkinson H, Heiman M, et al. (2021). Shape deformation analysis reveals the temporal dynamics of cell-type-specific homeostatic and pathogenic responses to mutant huntingtin. Elife 10, 1–25.

Menalled LB, Sison JD, Dragatsis I, Zeitlin S, and Chesselet MF (2003). Time course of early motor and neuropathological anomalies in a knock-in mouse model of Huntington's disease with 140 CAG repeats. J. Comp. Neurol 465, 11–26. [PubMed: 12926013]

Metsalu T, and Vilo J (2015). ClustVis: A web tool for visualizing clustering of multivariate data using Principal Component Analysis and heatmap. Nucleic Acids Res 43, W566–W570. [PubMed: 25969447]

Metzler M, Li B, Gan L, Georgiou J, Gutekunst CA, Wang Y, Torre E, Devon RS, Oh R, Legendre-Guillemin V, et al. (2003). Disruption of the endocytic protein HIP1 results in neurological deficits and decreased AMPA receptor trafficking. EMBO J 22+, 3254–3266. [PubMed: 12839988]

Metzler M, Gan L, Tak PW, Liu L, Helm J, Liu L, Georgiou J, Wang Y, Bissada N, Cheng K, et al. (2007). NMDA receptor function and NMDA receptor-dependent phosphorylation of huntingtin is altered by the endocytic protein HIP1. J. Neurosci 27, 2298–2308. [PubMed: 17329427]

Miteva YV, Budayeva HG, and Cristea IM (2013). Proteomics-based methods for discovery, quantification, and validation of protein-protein interactions. Anal Chem 85, 749–768. [PubMed: 23157382]

Nishi H, Fong JH, Chang C, Teichmann SA, and Panchenko AR (2013). Regulation of protein-protein binding by coupling between phosphorylation and intrinsic disorder: Analysis of human protein complexes. Mol. Biosyst 9, 1620–1626. [PubMed: 23364837]

Noel J, Ralph GS, Pickard L, Williams J, Molnar E, Uney JB, Collingridge GL, and Henley JM (1999). Surface expression of AMPA receptors in hippocampal neurons is regulated by an NSF-dependent mechanism. Neuron 23, 365–376. [PubMed: 10399941]

Ochaba J, Morozko EL, O'Rourke JG, and Thompson LM (2018). Fractionation for Resolution of Soluble and Insoluble Huntingtin Species. J. Vis. Exp 57082.

Onur TS, Laitman A, Zhao H, Keyho R, Kim H, Wang J, Mair M, Wang H, Li L, Perez A, et al. (2021). Downregulation of glial genes involved in synaptic function mitigates huntington's disease pathogenesis. Elife 10, 719–731.

Pal A, Severin F, Lommer B, Shevchenko A, and Zerial M (2006). Huntingtin-HAP40 complex is a novel Rab5 effector that regulates early endosome motility and is up-regulated in Huntington's disease. J. Cell Biol 172, 605–618. [PubMed: 16476778]

Perez-Riverol Y, Csordas A, Bai J, Bernal-Llinares M, Hewapathirana S, Kundu DJ, Inuganti A, Griss J, Mayer G, Eisenacher M, et al. (2019). The PRIDE database and related tools and resources in 2019: Improving support for quantification data. Nucleic Acids Res 47, D442–D450. [PubMed: 30395289]

Peters MF, and Ross CA (2001). Isolation of a 40-kDa Huntingtin-associated Protein. J. Biol. Chem 276, 3188–3194. [PubMed: 11035034]

Poudel GR, Harding IH, Egan GF, Georgiou-Karistianis N, Gary |, Egan F, Georgiou-Karistianis N, Egan GF, and Georgiou-Karistianis N (2019). Network spread determines severity of degeneration and disconnection in Huntington's disease. Hum. Brain Mapp 40, 4192–4201. [PubMed: 31187915]

Przytycka TM, Singh M, and Slonim DK (2010). Toward the dynamic interactome: It's about time. Brief. Bioinform 11, 15–29. [PubMed: 20061351]

Author Manuscript Author Manuscript Author Manuscript Author Manuscript

Ratovitski T, Chighladze E, Arbez N, Boronina T, Herbrich S, Cole RN, and Ross CA (2012). Huntingtin protein interactions altered by polyglutamine expansion as determined by quantitative proteomic analysis. Cell Cycle 11, 2006–2021. [PubMed: 22580459]

Ripaud L, Chumakova V, Antonin M, Hastie AR, Pinkert S, Körner R, Ruff KM, Pappu RV, Hornburg D, Mann M, et al. (2014). Overexpression of Q-rich prion-like proteins suppresses polyQ cytotoxicity and alters the polyQ interactome. Proc. Natl. Acad. Sci. U. S. A 111, 18219–18224. [PubMed: 25489109]

Romero E, Cha GH, Verstreken P, Ly CV, Hughes RE, Bellen HJ, and Botas J (2008). Suppression of Neurodegeneration and Increased Neurotransmission Caused by Expanded Full-Length Huntingtin Accumulating in the Cytoplasm. Neuron 57, 27–40. [PubMed: 18184562]

Ross CA, and Tabrizi SJ (2011). Huntington's disease: From molecular pathogenesis to clinical treatment (Lancet Neurol).

Saudou F, Humbert S, Dé Ric Saudou F, and Humbert S (2016). The Biology of Huntingtin. Neuron 89, 910–926. [PubMed: 26938440]

Scherzinger E, Lurz R, Turmaine M, Mangiarini L, Hollenbach B, Hasenbank R, Bates GP, Davies SW, Lehrach H, and Wanker EE (1997). Huntingtin-encoded polyglutamine expansions form amyloid-like protein aggregates in vitro and in vivo. Cell 90, 549–558. [PubMed: 9267034]

Scherzinger E, Sittler A, Schweiger K, Heiser V, Lurz R, Hasenbank R, Bates GP, Lehrach H, and Wanker EE (1999). Self-assembly of polyglutamine-containing huntingtin fragments into amyloid-like fibrils: Implications for Huntington's disease pathology. Proc. Natl. Acad. Sci. U. S. A 96, 4604–4609. [PubMed: 10200309]

Schilling G, Becher MW, Sharp AH, Jinnah HA, Duan K, Kotzuk JA, Slunt HH, Ratovitski T, Cooper JK, Jenkins NA, et al. (1999). Intranuclear inclusions and neuritic aggregates in transgenic mice expressing a mutant N-terminal fragment of huntingtin. Hum. Mol. Genet 8, 397–407. [PubMed: 9949199]

Scholz R, Berberich S, Rathgeber L, Kolleker A, Köhr G, and Kornau HC (2010). AMPA Receptor Signaling through BRAG2 and Arf6 Critical for Long-Term Synaptic Depression. Neuron 66, 768–780. [PubMed: 20547133]

Shannon P, Markiel A, Ozier O, Baliga NS, Wang JT, Ramage D, Amin N, Schwikowski B, and Ideker T (2003). Cytoscape: A software Environment for integrated models of biomolecular interaction networks. Genome Res 13, 2498–2504. [PubMed: 14597658]

Shirasaki DI, Greiner ER, Al-Ramahi I, Gray M, Boontheung P, Geschwind DH, Botas J, Coppola G, Horvath S, Loo JA, et al. (2012). Network organization of the huntingtin proteomic interactome in mammalian brain. Neuron 75, 41–57. [PubMed: 22794259]

Smith-Dijak AI, Sepers MD, and Raymond LA (2019). Alterations in synaptic function and plasticity in Huntington disease. J. Neurochem 150, 346–365. [PubMed: 31095731]

Song W, Chen J, Petrilli A, Liot G, Klinglmayr E, Zhou Y, Poquiz P, Tjong J, Pouladi MA, Hayden MR, et al. (2011). Mutant huntingtin binds the mitochondrial fission GTPase dynamin-related protein-1 and increases its enzymatic activity. Nat. Med 17, 377–383. [PubMed: 21336284]

Squitieri F, Frati L, Ciarmiello A, Lastoria S, and Quarrell O (2006). Juvenile Huntington's disease: Does a dosage-effect pathogenic mechanism differ from the classical adult disease? Mech. Ageing Dev 127, 208–212. [PubMed: 16274727]

Szklarczyk D, Morris JH, Cook H, Kuhn M, Wyder S, Simonovic M, Santos A, Doncheva NT, Roth A, Bork P, et al. (2017). The STRING database in 2017: Quality-controlled protein-protein association networks, made broadly accessible. Nucleic Acids Res 45, D362–D368. [PubMed: 27924014]

Szklarczyk D, Gable AL, Lyon D, Junge A, Wyder S, Huerta-Cepas J, Simonovic M, Doncheva NT, Morris JH, Bork P, et al. (2019). STRING v11: Protein-protein association networks with increased coverage, supporting functional discovery in genome-wide experimental datasets. Nucleic Acids Res 47, D607–D613. [PubMed: 30476243]

Tackett AJ, DeGrasse JA, Sekedat MD, Oeffinger M, Rout MP, and Chait BT (2005). I-DIRT, a general method for distinguishing between specific and nonspecific protein interactions. J Proteome Res 4, 1752–1756. [PubMed: 16212429]

Author Manuscript Author Manuscript Author Manuscript Author Manuscript

Tourette C, Li B, Bell R, O'Hare S, Kaltenbach LS, Mooney SD, and Hughes RE (2014). A large scale huntingtin protein interaction network implicates RHO GTPase signaling pathways in huntington disease. J. Biol. Chem 289, 6709–6726. [PubMed: 24407293]

Trepte P, Kruse S, Kostova S, Hoffmann S, Buntru A, Tempelmeier A, Secker C, Diez L, Schulz A, Klockmeier K, et al. (2018). Lu TH y: a double- readout bioluminescence-based two- hybrid technology for quantitative mapping of protein–protein interactions in mammalian cells. Mol. Syst. Biol 14.

Tsai Y-C, Greco TM, Boonmee A, Miteva Y, and Cristea IM (2012). Functional proteomics establishes the interaction of SIRT7 with chromatin remodeling complexes and expands its role in regulation of RNA polymerase I transcription. Mol. Cell. Proteomics 11, M111.015156.

Vanunu O, Magger O, Ruppin E, Shlomi T, and Sharan R (2010). Associating genes and protein complexes with disease via network propagation. PLoS Comput. Biol 6, e1000641. [PubMed: 20090828]

Veldman MB, and Yang XW (2018). Molecular insights into cortico-striatal miscommunications in Huntington's disease. Curr. Opin. Neurobiol 48, 79–89. [PubMed: 29125980]

Vonsattel JPG (2008). Huntington disease models and human neuropathology: Similarities and differences. Acta Neuropathol 115, 55–69. [PubMed: 17978822]

Waldvogel HJ, Kim EH, Tippett LJ, Vonsattel JPG, and Faull RLM (2014). The neuropathology of Huntington's disease. Curr. Top. Behav. Neurosci 22, 33–80.

Wang Y, Meriin AB, Zaarur N, Romanova NV, Chernoff YO, Costello CE, and Sherman MY (2009). Abnormal proteins can form aggresome in yeast: aggresome- targeting signals and components of the machinery. FASEB J 23, 451–463. [PubMed: 18854435]

Wanker EE, Ast A, Schindler F, Trepte P, and Schnoegl S (2019). The pathobiology of perturbed mutant huntingtin protein–protein interactions in Huntington's disease. J. Neurochem 151, 507–519. [PubMed: 31418858]

Welch MD, DePace AH, Verma S, Iwamatsu A, and Mitchison TJ (1997). The human Arp2/3 complex is composed of evolutionarily conserved subunits and is localized to cellular regions of dynamic actin filament assembly. J. Cell Biol 138, 375–384. [PubMed: 9230079]

Wilkens S, Inoue T, and Forgac M (2004). Three-dimensional structure of the vacuolar ATPase: Localization of subunit h by difference imaging and chemical cross-linking. J. Biol. Chem 279, 41942–41949. [PubMed: 15269204]

Wiśniewski JR, Zougman A, Nagaraj N, and Mann M (2009). Universal sample preparation method for proteome analysis. Nat. Methods 6, 359–362. [PubMed: 19377485]

Wong YC, and Holzbaur ELF (2014). The regulation of autophagosome dynamics by huntingtin and HAP1 is disrupted by expression of mutant huntingtin, leading to defective cargo degradation. J. Neurosci 34, 1293–1305. [PubMed: 24453320]

Wu PG, and Brand L (1994). Resonance energy transfer: Methods and applications. Anal. Biochem 218, 1–13. [PubMed: 8053542]

Zhang H, Zhang C, Vincent J, Zala D, Benstaali C, Sainlos M, Grillo-Bosch D, Daburon S, Coussen F, Cho Y, et al. (2018). Modulation of AMPA receptor surface diffusion restores hippocampal plasticity and memory in Huntington's disease models. Nat. Commun 9.

Zhao Y, Zurawel AA, Jenkins NP, Duennwald ML, Cheng C, Kettenbach AN, and Supattapone S (2018). Comparative Analysis of Mutant Huntingtin Binding Partners in Yeast Species. Sci. Rep 8.

Zheng S, Ghitani N, Blackburn JS, Liu JP, and Zeitlin SO (2012). A series of N-terminal epitope tagged Hdh knock-in alleles expressing normal and mutant huntingtin: Their application to understanding the effect of increasing the length of normal huntingtins polyglutamine stretch on CAG140 mouse model pathogenesis. Mol. Brain 5.

Zhu W, Smith JW, and Huang CM (2010). Mass spectrometry-based label-free quantitative proteomics. J. Biomed. Biotechnol 2010.

Author Manuscript Author Manuscript Author Manuscript Author Manuscript

## Highlights

- Profiled perturbed protein interactions in striatum of Huntington's disease model
- Classified differentially stabilized or dynamic mutant huntingtin protein interactions
- Defined direct mutant huntingtin interacting partners in human HD cell model
- Tested the link between HTT interactions and disease progression in HD fly model

Author Manuscript Author Manuscript Author Manuscript Author Manuscript

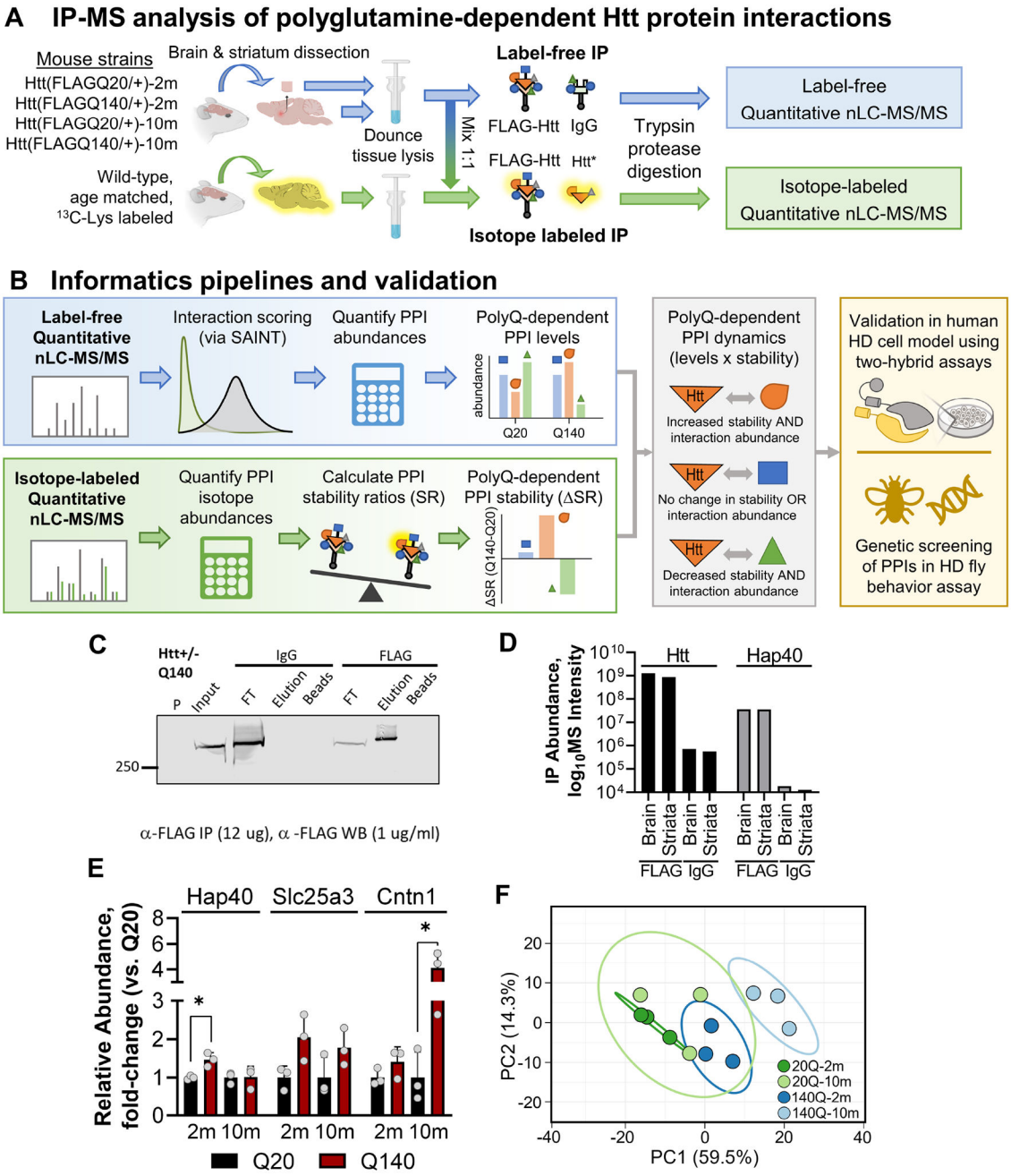


**Figure 1. Htt protein complexes isolated from the mouse striatum at two ages were quantified by label-free and metabolic labeling immunoaffinity purification-mass spectrometry.**

(A) Label-free quantitative IP-MS workflow evaluated Htt interaction specificity and polyQ length-dependence. (B) Computational workflow integrating label-free (LF) and isotope-labeled (IL) quantitative IP-MS experiments. The LF arm of the workflow (blue box) determined PPI candidates that were specific interactions (SAINT) and their respective polyQ length-dependence (MS1-based peak area). The IL arm of the workflow (green box) determined the poly length-dependence of the PPI candidates' relative stability. This was performed by quantifying light (endogenous) and heavy (spike-in standard) isotope abundances, then calculating the PPI stability ratios, SR = [light / (light + heavy)], and

Author Manuscript Author Manuscript Author Manuscript Author Manuscript

finally, the difference in stability ratios (ΔSR) between age-matched Q140 and Q20 genotypes. The possibility for changes in PPI levels and/or stability can produce different types of interaction dynamics (grey box). Dynamic PPIs were selected for functional validation by orthogonal assays (yellow box). (C) The efficiency of FLAG-Htt-Q140 extraction and immunoisolation (IP) from mouse brain tissue was monitored by western blot analysis of the insoluble (P) and soluble (Input) fractions, and the IP flow-through (FT), Elution, and Bead fractions. (D) Htt and Hap40 protein abundances measured by MS using summed peptide intensities were compared between FLAG-Htt and IgG IPs in the brain and striata of Q140–2m tissues (n = 1). (E) Quantification of known Htt PPIs co-isolated by FLAG-Htt IP from striatal tissues. Relative PPI abundances were expressed versus age matched, Q20 controls (mean ± SD, n=3). PolyQ-dependent increases in Hap40 association at 2m (~40%) and contactin 1 at 10m (4-fold) were statistically significant (*, $p < 0.05$, unpaired t-test). (F) Principal component analysis of SAINT filtered Htt interaction abundances calculated by $MS^1$-based label-free quantification (see STAR methods) as a function of polyQ length and age. Note, throughout the study, when reporting results involving human or mouse proteins, we use different capitalization, e.g., HTT and Htt to denote the huntingtin protein from human and mouse models, respectively.

Author Manuscript Author Manuscript Author Manuscript Author Manuscript

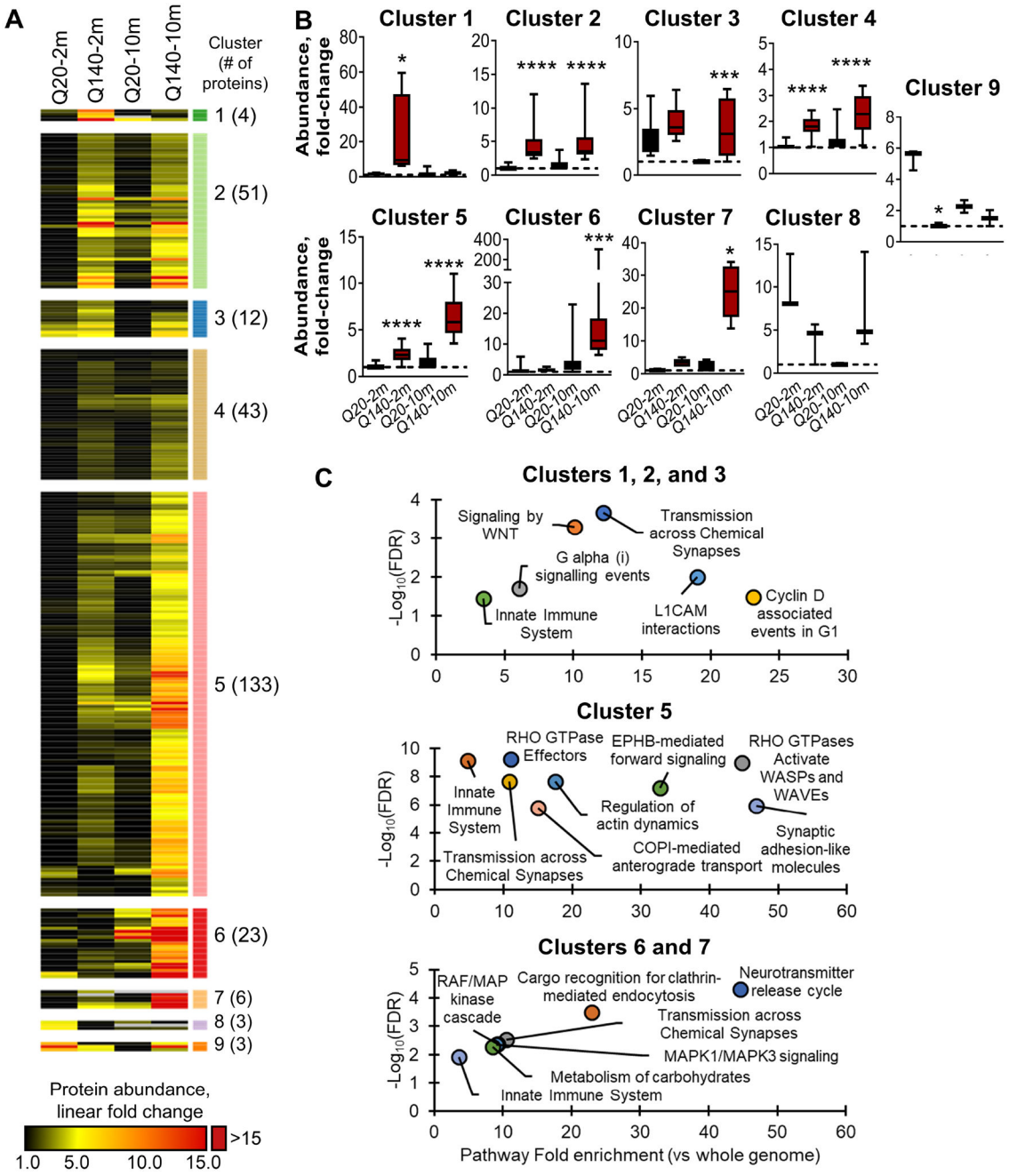


**Figure 2. Htt interactions show distinct changes as a function of age and polyQ length.**

(A) Hierarchical clustering of Htt protein interactions. Proteins that passed the SAINT filter (score > 0.8) in at least one condition (n =278) were clustered by Pearson's correlation with average linkage using normalized protein abundances (linear), calculated by normalizing raw abundances to bait (Htt) abundances, then to the row minimum of Htt-normalized abundance. Missing values are indicated in grey. The number of proteins in each cluster are indicated in parentheses. (B) Relative protein abundance fold-change values from the heatmap were summarized at the cluster level as box and whisker plots (median ± IQR; whiskers: 5–95% confidence). A non-parametric Kruskal-Wallis test, followed by a Dunn's

multiple comparison post-test was used to determine statistical significance of Q140 versus Q20 for 2m and 10m sample groups (n = see heatmap cluster; *, $p < 0.05$; ***, $p < 0.001$; ****, $p < 0.0001$). (C) Statistical over-representation of Reactome pathway for selected clusters, expressed in terms of enrichment confidence (FDR) and fold-change enrichment (versus the total genome) for each pathway term.

Author Manuscript Author Manuscript Author Manuscript Author Manuscript

Author Manuscript Author Manuscript Author Manuscript Author Manuscript

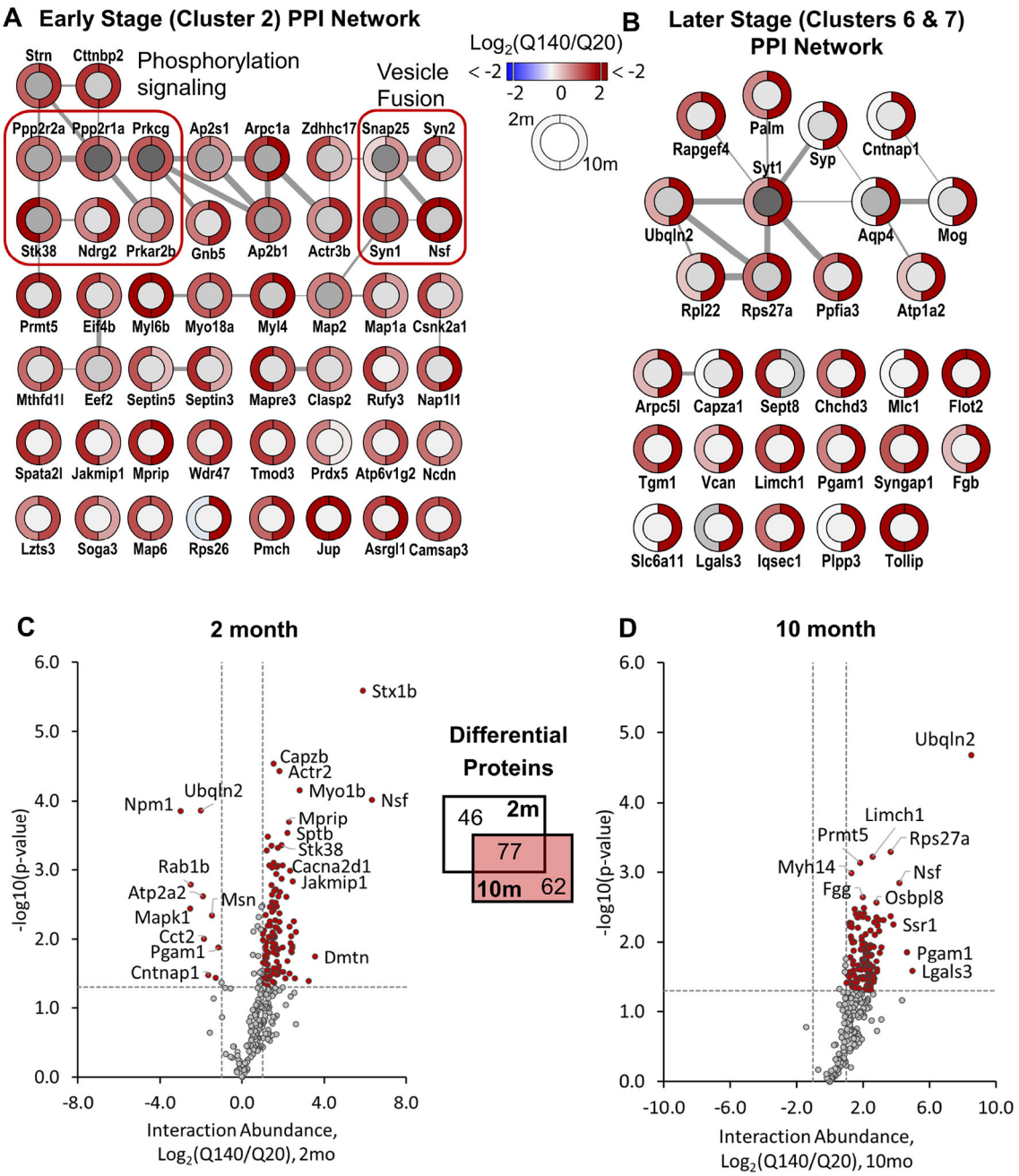


**Figure 3. mHtt-dependent functional networks and differential PPIs in 2m and 10m mice.**

(A & B) STRING network of Htt PPIs assigned to (A) clusters 2 or (B) clusters 6 and 7 in Fig 2A. Node donut color gradients indicate relative PPI abundances, $\log_2$(Q140/Q20), at 2 (left) and 10 months (right). Node circle fill gradient from light to dark indicates low to high degree of connectivity, respectively. Edge width indicates STRING interaction score (0.4 – 1.0) (C & D) PolyQ-dependent Htt PPIs (red dots) were determined by reproducibility of interaction (p-value < 0.05, student's t-test, n=3) and change in interaction abundance (±1.0 fold, $\log_2$) in 2m and 10m mice. Overlap of polyQ-dependent PPIs is indicated by the Venn diagram

Author Manuscript Author Manuscript Author Manuscript Author Manuscript

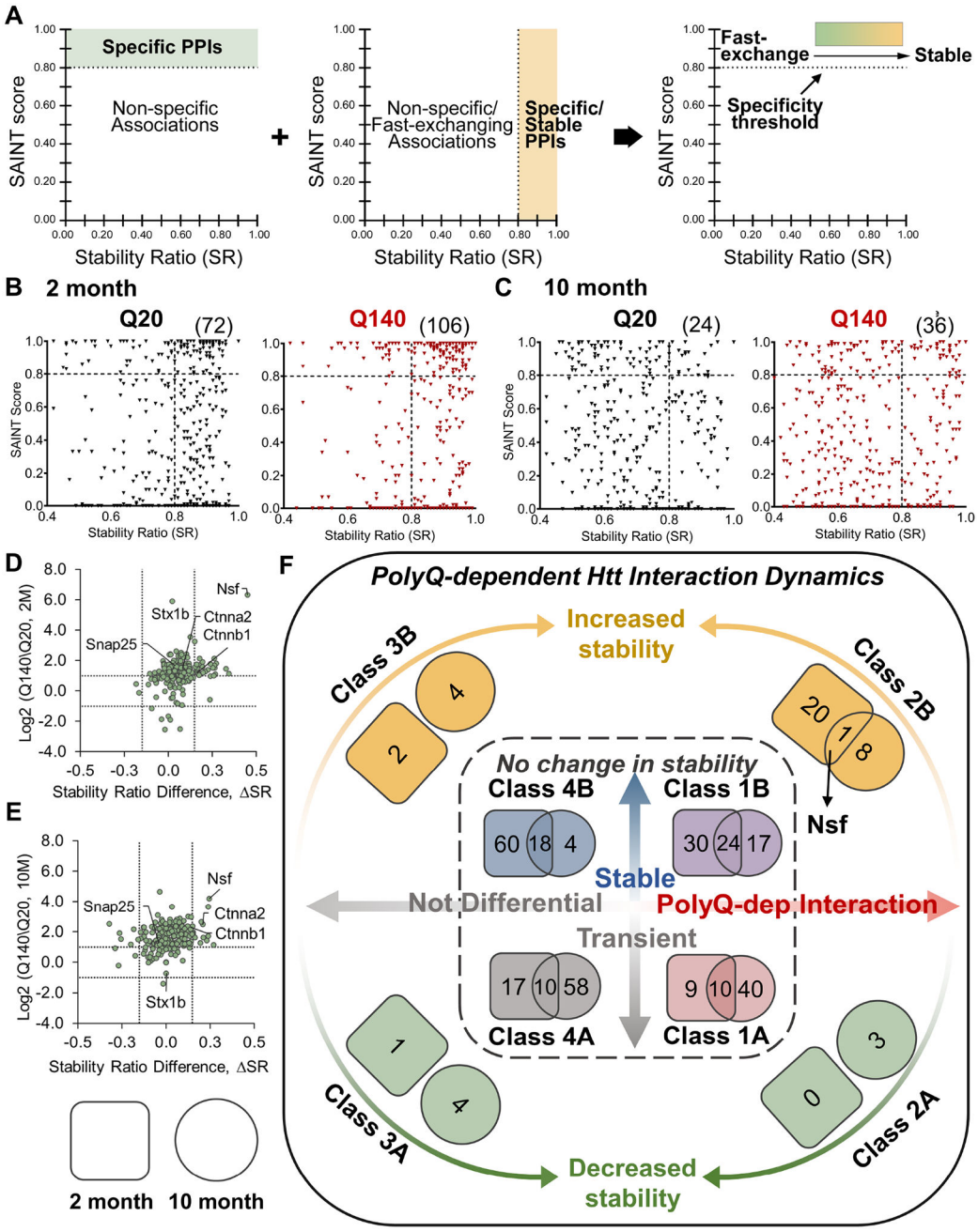


**Figure 4. Profiling the stability landscape of Htt interactions in the striatum through complementary IP-MS approaches.**

(A) Integration of specificity (SAINT score) and stability (stability ratio, SR) measurements for evaluating PPI dynamics. For each condition, a continuum of PPI relative stabilities was defined by applying a label-free specificity threshold of 0.8 and an SR threshold of 0.8. (B & C) Protein interaction specificity versus stability for proteins quantified by label-free and metabolic labeling IP-MS, respectively. The number of proteins that were stable and specific Htt PPIs are shown in parentheses (upper-right quadrant). (D & E) Scatterplot comparison of polyQ length-dependent (Q140 vs Q20) change in PPI abundance (y-axis) and stability ratio difference (x-axis) in 2- (D) and 10-month-old mice (E). PolyQ length-dependent

Author Manuscript Author Manuscript Author Manuscript Author Manuscript

thresholds are indicated by dashed lines. (F) Htt PPI dynamics were assigned into one of four primary (1 – 4) and two secondary classes (A or B) according to polyQ-dependent interaction levels and relative stability. PPIs either showed no polyQ-dependency in their relative stabilities, i.e. they maintain stable (Class 1B/4B) or transient (Class 1A/4A) type), and had interaction abundances that were polyQ-dependent (Class 1) or not (Class 4), or they showed increases (Class 2B/3B) or decreases (Class 2A/3A) in relative stabilities and had interaction abundances that were polyQ-dependent (Class 2) or not (Class 3). The number of proteins assigned to each class by mouse model age (2m and 10m) are indicated by Venn overlap (square and circle, respectively).

Author Manuscript Author Manuscript Author Manuscript Author Manuscript

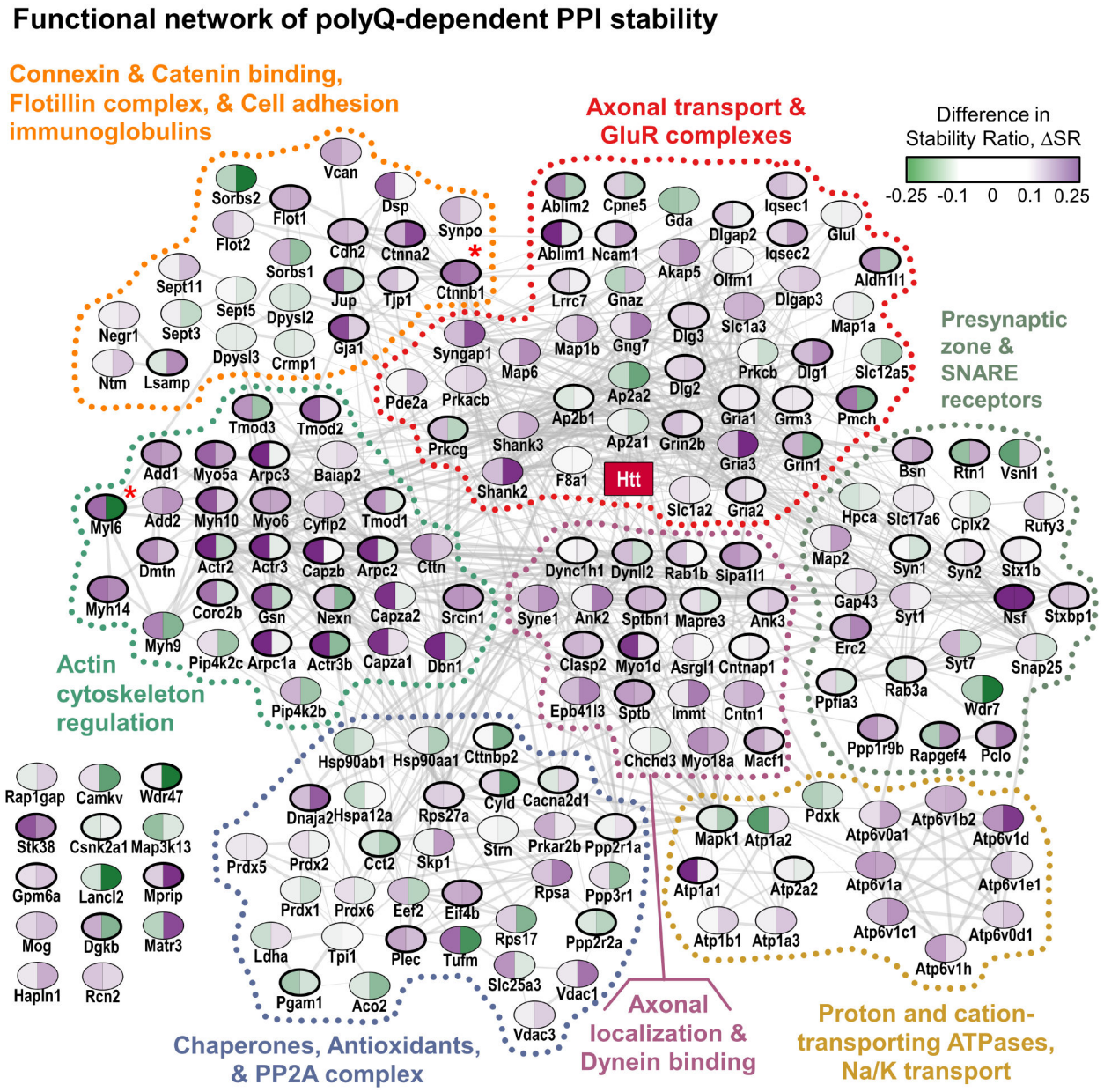


**Figure 5. Mutant Htt-dependent increases in relative stability predominate at 2m and in specific functional modules.**

An interaction network was assembled based on the STRING database (score ≥ 0.5, edge thickness) for the 201 Htt PPIs that had measured abundances and relative stabilities. Clusters (*dotted lines*) were assigned by connectivity using ReactomeFI and over-represented functions were determined by STRING functional enrichment (see Fig S5A). PolyQ-dependent changes in interaction stability (ΔSR) were visualized by node color gradients for 2m (*left*) and (*right*) 10m ages. PPIs with polyQ-dependent differential levels (see Fig 4 and Table S2) are indicated by bold node border.

Author Manuscript Author Manuscript Author Manuscript Author Manuscript

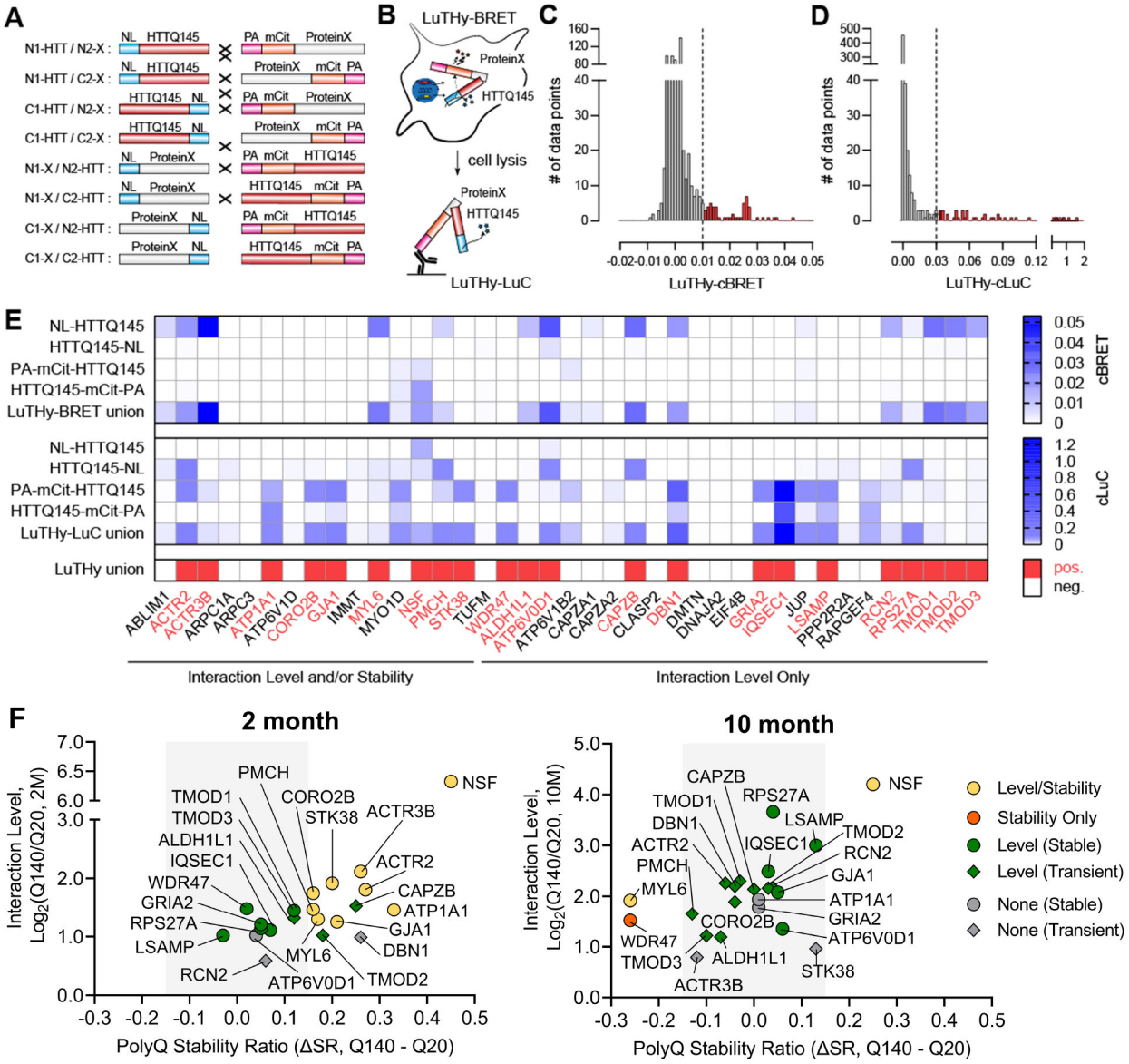


**Figure 6. LuTHy two-hybrid assays in a human HD cell model validate Htt PPIs identified by IP-MS in mouse striatum.**

(A) Fusion protein constructs and tagging configurations used in LuTHy validation. HTTQ145 and selected PPIs identified by IP-MS (ProteinX) were tested as donors tagged with Nanoluciferase (NL) and acceptors tagged with mCitrine and Protein-A (PA-mCit/ mCit-PA) (Table S8). Each interaction was tested in all of the 8 possible orientations. (B) Graphical illustration and workflow of the two readouts of LuTHy: in-cell bioluminescence energy transfer (LuTHy-BRET) and luciferase co-precipitation (LuTHy-LuC) after cell lysis. (C, D) Distribution of all data points for corrected LuTHy-BRET (LuTHy-cBRET, C) and corrected LuTHy-LuC (LuTHy-cLuC, D). Interactions were scored positive if cBRET ≥ 0.01 and/or cLuC ≥ 0.03 (red bars). (E) Heatmap of in-cell LuTHy-cBRET and -cLuC values for human orthologues of PPIs identified by IP-MS that were screened against human HTTQ145. NL-HTTQ145 and HTTQ145-NL were tested against N- and C-terminally PA-

Author Manuscript Author Manuscript Author Manuscript Author Manuscript

mCit-tagged proteins, and vice versa for PA-mCit/mCit-PA-tagged HTTQ145. Each PPI square denotes the highest cBRET and cLuc values of the candidate protein tested against the specific HTT tagging orientation. The LuTHy union row was scored positive (*red squares and text*) if the interaction score was above threshold in at least one orientation in either the LuTHy-LuC or LuTHy-BRET readouts. (F) Comparison of polyQ length-dependent change in interaction levels and stability in Q20 and Q140 mice at 2M (*left*) and 10M (right) for LuTHy-validated proteins.

Author Manuscript Author Manuscript Author Manuscript Author Manuscript

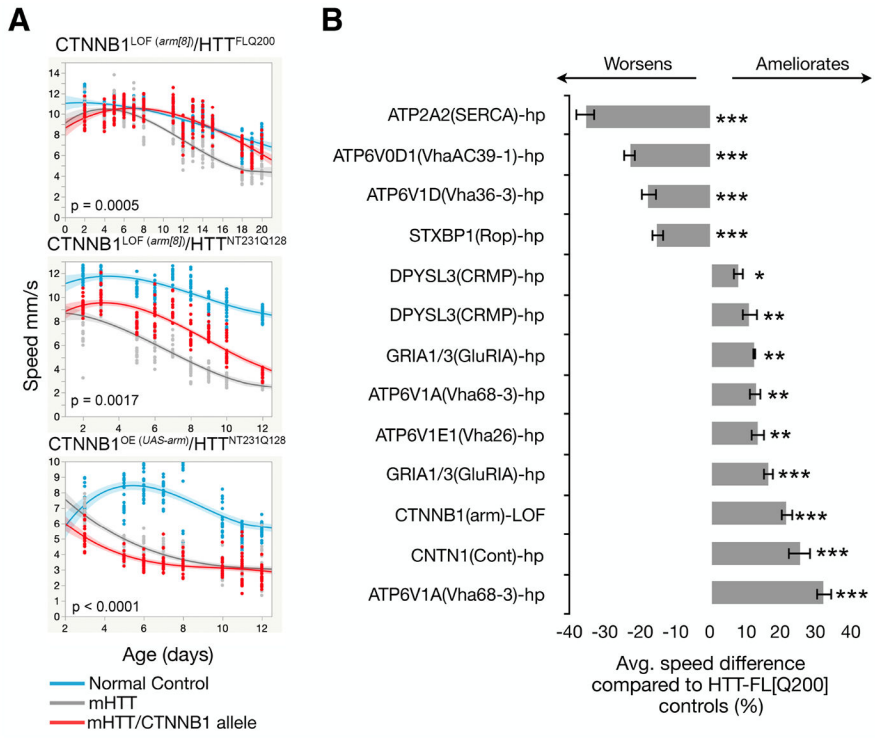


C

| Protein Description | Human Gene Symbol | Prior Genetic Modifier Evidence[1] | HTT length (FL/Frag)[2] | Interaction Class[3] | Functional Class[4] |
|---|---|---|---|---|---|
| Catenin beta-1 | CTNNB1 | fly, worm, cell | Frag | Level+ Stability | Cell-cell adhesion |
| Contactin-1 | CNTN1 | - | - | Level only | Axonal localization |
| Dihydropyrimidinase-related protein 3 | DPYSL3 | fly, cell | FL / Frag | Level only | Cell-cell adhesion |
| Glutamate receptor 1 | GRIA1 | fly | Frag | Level only | Axon Transport & GluR |
| Glutamate receptor 3 | GRIA3 | fly | Frag | Stability only | Axon Transport & GluR |
| Sarcoplasmic/endoplasmic reticulum calcium ATPase 2 | ATP2A2 | fly | Frag | Level only | ATPases |
| Syntaxin-binding protein 1 | STXBP1 | fly, cell | FL / Frag | Level only | SNAREs/Pre-synaptic zone |
| V-type proton ATPase catalytic subunit A | ATP6V1A | fly, worm | Frag | Level only | ATPases |
| V-type proton ATPase subunit D | ATP6V1D | - | - | Level+ Stability | ATPases |
| V-type proton ATPase subunit d 1 | ATP6V0D1 | - | - | Level only | ATPases |
| V-type proton ATPase subunit E 1 | ATP6V1E1 | worm | Frag | Level only | ATPases |

**Figure 7. HTT PPIs modulate mHTT-induced neuronal dysfunction in vivo.**

(A) Charts showing speed (mm/s) as a function of age in non-disease control fruit flies (*blue*), disease control flies expressing mHTT only in neurons (*grey*), or experimental animals expressing mHTT in neurons and also carrying the indicated allele in *armadillo*, the *Drosophila Ctnnb1* homolog (*red*). Each line is a 3rd degree polynomial regression, shading represents confidence intervals. (B) Bar chart showing the average worsening or amelioration (%) of neuronal dysfunction measured as a climbing speed difference. The data represents *Drosophila* expressing $HTT^{FL[Q200]}$ with each of the shown alleles in the *Drosophila* homologs of the indicated mHTT interactors. *Drosophila* expressing

Author Manuscript Author Manuscript Author Manuscript Author Manuscript

$HTT^{FL[Q200]}$ and a control non-targeting hairpin RNA were used as the reference. The effect of all modifiers was statistically significant following mixed models ANOVA. Error bars in B correspond to the standard error of the mean. LOF: loss of function / +. hp: hairpin RNA. OE: Overexpression. * $p<0.05$, ** $p<0.01$, *** $p<0.001$. Specific genotypes and p values are shown in Table S9. (C) Annotated table of genetic modifiers in B. [1]Identified as genetic modifier in this study (fly) or prior studies in cells, fly, worm, mouse, and/or human HD models (see Table S7 for full annotations and references). [2]Indicates whether the HD model system(s)[1] used full length (FL) or fragment (Frag) HTT. [3]Assignment of PPI as polyQ-dependent in interaction level, stability, or level+stability in this study (see Table S4). [4]Indicates the functional module from the HTT interactome network (see Fig 5).

Author Manuscript Author Manuscript Author Manuscript Author Manuscript

## Key resources table

| REAGENT or RESOURCE | SOURCE | IDENTIFIER |
|---|---|---|
| Antibodies | | |
| Mouse monoclonal anti-FLAG M2 | MilliporeSigma | Cat# F3165; RRID: AB_259529 |
| Mouse IgG, lyophilized | MP Biomedical | Cat# 0864146-CF |
| Goat anti-mouse Alexa Fluor 680 | ThermoFisher Scientific | Cat#A-21058; RRID: AB_2535724 |
| Bacterial and virus strains | | |
| MultiShot™ StripWell Mach1™ T1 Phage-Resistant Chemically Competent E. coli | Invitrogen | C869601 |
| Chemicals, peptides, and recombinant proteins | | |
| 2-Methylbutane | Fisher Scientific | Cat#O3551-4 |
| Halt protease and phosphatase inhibitors | ThermoFisher Scientific | Cat#78446 |
| Universal nuclease | ThermoFisher Scientific | Cat#88701 |
| Linear polyethyleneimine, 25 kDa | Polysciences | Cat#23966 |
| TCEP-HCl, no-weigh | ThermoFisher Scientific | Cat#20491 |
| 2-Chloroacetamide | MilliporeSigma | Cat#22790 |
| Coelenterazine | pjk GmbH | 102171 |
| Biological samples | | |
| Mouse Express BRAIN TISSUE | Cambridge Isotope | Cat# MT-LYSC6-MB-PK |
| Critical commercial assays | | |
| Gateway™ LR Clonase™ II Enzyme mix | Invitrogen | 11791020 |
| Deposited data | | |
| Raw and analyzed mass spectrometry data | This paper; ProteomeXchange | PXD025510 |
| Raw mass spectrometry data from proteome analyses of striatum tissue from allelic series HD mice | Langfelder et al. 2016 | http://proteomecentral.proteomexchange.org/cgi/GetDataset?ID=PXD003442 |
| Experimental models: Cell lines | | |
| Human: HEK-293 cells | DSMZ-German Collection of Microorganisms and Cell Cultures GmbH | CVCL_0045; DMSZ no.: ACC 305 |
| Experimental models: Organisms/strains | | |
| *D. melanogaster: UAS*-HTT$^{FL[Q200]}$ | Romero et al., 2008 | N/A |
| *D. melanogaster: UAS*-HTT$^{NT231[Q128]}$ | Onur et al., 2021 | N/A |
| Mouse: *Htt*3xFlag20Q/+ | Zheng et al., 2012 | N/A |
| Mouse: *Htt*3xFlag140Q/+ | Zheng et al., 20212 | N/A |
| Recombinant DNA | | |
| pcDNA3.1 NL | Trepte et al. 2018 | Addgene #113442 |
| pcDNA3.1 PA-mCit | Trepte et al. 2018 | Addgene #113443 |
| pcDNA3.1 PA-mCit-NL | Trepte et al. 2018 | Addgene #113444 |
| pcDNA3.1 PA-NL | Trepte et al. 2018 | Addgene #113445 |
| pcDNA3.1 myc-NL-GW | Trepte et al. 2018 | Addgene #113446 |

Author Manuscript Author Manuscript Author Manuscript Author Manuscript

| REAGENT or RESOURCE | SOURCE | IDENTIFIER |
|---|---|---|
| pcDNA3.1 GW-NL-myc | Trepte et al. 2018 | Addgene #113447 |
| pcDNA3.1 PA-mCit-GW | Trepte et al. 2018 | Addgene #113448 |
| pcDNA3.1 GW-mCit-PA | Trepte et al. 2018 | Addgene #113449 |
| Human ORFeome V5.1 collection | Lamesch et al. 2007 | Center for Cancer Systems Biology (CCSB), Dana-Farber Cancer Institute |
| RZPD cDNA library | Zehetner and Lehrach 1994 | Resource Center and Primary Database (RZPD) |
| LuTHy expression vectors | This paper | Table S8 |
| Plasmids for Drosophila motor performance assays | This paper | Table S9 |
| Software and algorithms | | |
| Proteome Discoverer | ThermoFisher Scientific | Ver. 2.2.0.388 |
| SAINT | Choi et al., 2011 | http://reprint-apms.org |
| Cytoscape | Shannon et al., 2003 | http://www.cytoscape.org |
| STRING | Szklarczyk et al., 2017 | http://www.string-db.org |
| Panther | Panther Classification System | http://pantherdb.org/ |
| ClueGO | Bindea et al., 2009 | http://www.ici.upmc.fr/cluego/ |
| Morpheus | Broad Institute | https://software.broadinstitute.org/morpheus/ |
| Clustvis | Metsalu and Vilo, 2015 | https://github.com/taunometsalu/ClustVis |
| Graphpad Prism | https://www.graphpad.com | Prism 9 |
| Other | | |
| Amicon Ultra-0.5 Centrifugal Filter, Ultracel-30 | MilliporeSigma | Cat#UFC503096 |
| ReproSil-Pur 120 C18-AQ 1.9um | Dr. Maisch, GmbH | Cat#r119.aq.0001 |